Neutron-proton charge-exchange scattering between 600 and 2000 MeV/c †

P. F. Shepard,* T. J. Devlin,‡ R. E. Mischke,§ and J. Solomon‖
Joseph Henry Laboratories, Princeton University, Princeton, New Jersey 08540
(Received 10 June 1974)

n-p elastic differential cross sections in the charge-exchange region have been measured for incident neutron momenta between 600 and 2000 MeV/c. The momentum of neutrons incident on a liquid-H_2 target was determined by a measurement of flight time over a 32.9-m flight path. The momentum and scattering angles of the recoil proton were measured by a wire-spark-chamber magnetic spectrometer. Approximately 450 000 elastic events were detected for proton laboratory angles between 0° and 62°. Differential cross sections are presented at 16 energies. An absolute normalization of the cross sections was achieved by measuring the incident neutron flux with a detector whose efficiency was determined experimentally.

I. INTRODUCTION

The importance of new experimental information about the nucleon-nucleon interaction needs little emphasis. The data have been used primarily as input to a phase-shift analysis for comparison with theoretical models as they are proposed. Such analyses are especially involved because of the spin-$\frac{1}{2}$ character of the nucleon, and because they require a complete set of scattering data. Even though phase-shift analyses have been extensively pursued at two laboratories in particular, Livermore[1-4] and Yale,[5,6] a unique solution for n-p scattering exists only for 142, 210, and 425 MeV.[4]

The experiment described in this paper investigates the n-p charge-exchange differential cross section in a momentum region which has not been studied in detail previously. It covers the range from below the threshold for one-pion production (810 MeV/c) to up to a laboratory momentum of 2 GeV/c. The experiment was performed at the Princeton-Pennsylvania Accelerator (PPA) using a neutron beam which contained a broad spectrum of momenta. Time of flight (TOF) was used to determine the momenta of individually scattered neutrons. The momenta and scattering angles of recoiling protons were measured with a wire-chamber spectrometer. The combined TOF and spectrometer information was used to determine the mass of the missing part of the system. Elastic n-p scattering events were chosen on the basis of this mass test. The absolute flux of incident neutrons was measured by TOF with a detector whose efficiency was determined experimentally (and checked with a Monte Carlo calculation). This allowed a determination of the absolute normalization of the differential cross sections.

This paper presents the details of the experiment and the complete data set. It incorporates the results of a reanalysis of the data made after two previous reports.[7,8] There are some small quantitative changes in the final results presented here, but the principal features of the earlier reports are unchanged. In one of those[7] we presented only the main features of the backward differential cross section at very small momentum transfers. It was this portion of the charge-exchange cross section which showed sharp peaking in two early high-energy experiments.[9,10] Wilson[11] noted that this general shape is also present in the low-energy data.

This experiment was designed to investigate the sharp peaking in the backward direction as well as provide a large amount of data on the detailed behavior of the elastic cross section over a wide angular range. Our data not only confirm that the sharp peaking is present throughout our momentum region but also show that the peaking has an energy dependence with a maximum slope at a momentum of ~800 MeV/c. Recent experiments have extended the data to higher energies.[12-14]

Considerable effort has been invested into attempts to gain a theoretical understanding of the n-p charge-exchange process, but with only limited success.[15-18] Boson-exchange models[19,20] obtain reasonable agreement with the low-energy data but do not extend to above the inelastic threshold. Other models fit the data at high energies[21,22] but are not applicable at lower energies. Most theorists seem to agree that the sharp peaking is due to an interference between the one-pion exchange amplitude with a slowly varying background. An adequate theory of the background amplitude over the full momentum range does not exist and there is even some conflict about the data.[23,24]

II. EXPERIMENTAL DETAILS

A. The synchrotron

The maximum proton kinetic energy of the PPA was 3.0 GeV, and the repetition rate was one mag-

net cycle per 53 msec. The target spill for our experiment occurred over an 8-msec period centered about the maximum energy point of the magnet cycle. There were four rf acceleration cavities operating at a frequency of ~30 MHz at the peak of each acceleration cycle. Their frequency is the eighth harmonic of the proton orbit frequency and thus eight phase-stable regions, called bunches or buckets, circulate around the circumference. Since the rf frequency was large, the bunches were only ~60 cm in length and ~2 nsec in time-width near maximum energy.

The time-width of the protons striking the target was actually less than that of the bunches in stable orbit for the particular targeting technique used during our experiment. Kitagaki[25] estimated the time-width to be approximately 0.7 nsec and Stovink[26] measured 1.06 nsec.

The timing ambiguities associated with measuring TOF modulo ~33 nsec were so severe that the synchrotron was commonly operated in a manner so as to increase the natural bunch spacing to 67 nsec. This was accomplished through the electrostatic deflection of alternate bunches at injection time. The chopping system was not perfectly efficient, and the "empty" bunches contained some protons. A long-term time average of the contamination was kept throughout the experiment (see Sec. II C). During the actual data-taking, contaminations were found to be generally on the order of 0.1% (consistent with the noise level of the measuring system) and in a few cases as high as 0.5%. This contamination was negligible as a correction to the data.

It was also possible to operate the synchrotron with ~134-nsec structure by adjusting the chopper to exclude three out of every four proton bunches. Measurements of our incident neutron spectrum were made with the synchrotron operated in this mode. The neutron production spectrum was independent of the chopper operation mode.

B. The neutron beam

Figure 1 shows the layout of the secondary beam used in this experiment. Our liquid-H_2 (LH_2) target was located at 32.9 m. The flight-path length was chosen as a compromise between achieving good resolution at high incident momentum and the desire to have neutrons whose incident momentum is below the inelastic threshold arrive within ~67 nsec after the γ's produced by the same internal proton bunch. This was done because of the ambiguity in deciding which bunch of protons produced the neutron under study. For example, a sufficiently low-energy neutron could be overtaken by a higher-energy neutron produced ~67 nsec later. The elastic scattering of such a low-energy neutron is indistinguishable in our experiment from a high-energy inelastic scattering. As the distance from the production target increases, the energy at which this ambiguity occurs increases. Therefore, since we required our data to extend into the energy region below the inelastic threshold, the flight path was constrained to be no greater than approximately 32.9 m.

The beam was taken at an angle of 34° with respect to the internal proton beam. It was a simple neutral beam with a solid angle of 0.378 μsr. Our measurements showed ~30 neutrons per 10^{10} circulating protons emerged from the internal target into our beam with momenta between 600 and 2000 MeV/c. The polarization of the incident neutron beam was measured at energies of 300 and 570 MeV. An average value of the polarization of $(-4.7\pm1.4)\%$ was obtained.[27] This small polarization was neglected as a correction to the data. There were approximately an equal number of γ's and a negligible number of K_2^0 mesons (~1/1000 the number of neutrons). The γ's were largely removed with a 5-cm lead filter located 3.8 m from the production target.

The internal Pt target was 3.8 cm long, and

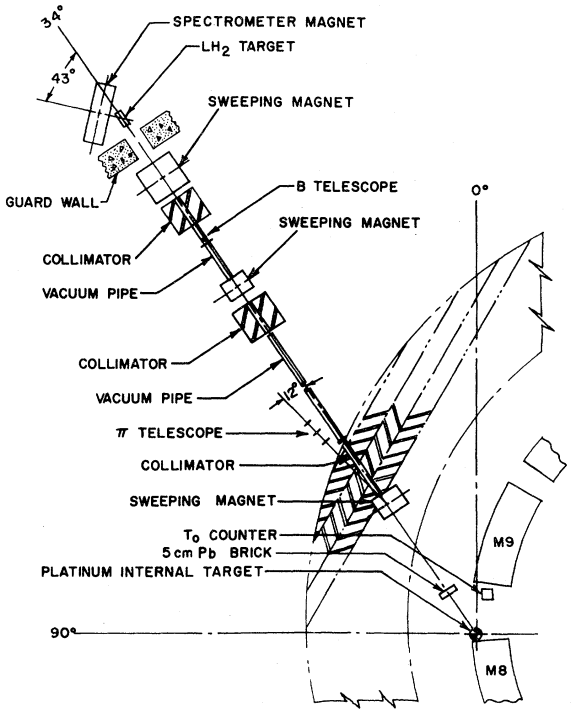

FIG. 1. Schematic plan view of the experimental arrangement. The spectrometer is shown in the wide-angle configuration. For clarity a large midsection of the beam line and some of the shielding have been omitted.

1.27×0.635 cm^2 in cross section. The limiting aperture of the defining collimator was located at 23 m. The collimator consisted of a 1.52-m piece of steel with a cylindrical hole 1.59 cm in diameter. Another 1.52-m steel collimator with a circular aperture 3.49 cm in diameter was used to eliminate lip scattering from the first collimator. Its defining aperture was located 27.4 m from the target. A sweeping magnet was located in the shielding wall of the synchrotron and was also used to produce the positively-charged unfocused beam whose use is discussed below. Two other sweeping magnets were located immediately after the two collimators in the beam. The beam interacted only with air between the last sweeping magnet and the LH_2 target, thus it was assumed that only neutral particles were incident on the LH_2 target.

Beam profiles were taken at a point 32.9 m from the production target using a small probe counter. The horizontal beam distribution in the median plane consisted of an umbra 1.14 cm in width and a penumbra of 1.27 cm on either side. The vertical beam distribution at the center line was not measurably different. The measured beam distribution was in excellent agreement with the expected profile based on the collimator geometry. Both distributions were centered in agreement with the final surveyed position of the defining collimator. We did not detect any beam halo, and an upper limit of the ratio of halo to beam per unit solid angle of 0.005 was established. The angular divergence of the beam at 32.9 m was less than 0.1 mrad.

The LH_2 target used in the experiment consisted of a Mylar flask 5.08 cm in diameter and 35.6 cm long. When filled with LH_2, the target had a thickness of ~2.5 g/cm^2. The end of the LH_2 flask closest to the synchrotron was positioned 32.91 m from the production target. The walls of the flask were Mylar and 0.19 mm thick. The flask was insulated with 25 layers of 6.4-μm Mylar coated with 0.02 μm of Al. The neutron beam entered and left the assembly through Mylar windows 0.64 mm thick (Figs. 2 and 3).

Three monitors were used in the experiment. The first, called BOT (beam on target), was a three-counter charged-particle telescope located inside the synchrotron ring at 90° with respect to the production target. Its counting rate was ~3–4 counts per 10^{10} protons onto a 3.8-cm Pt target. The second, called B, was located in the neutron beam in front of the second collimator (Fig. 1). It consisted of an anticoincidence counter, a 1.9-cm-thick polyethylene converter, and two coincidence counters.[28] All the counters were constructed from 1.59-mm scintillator, and the limiting coun-

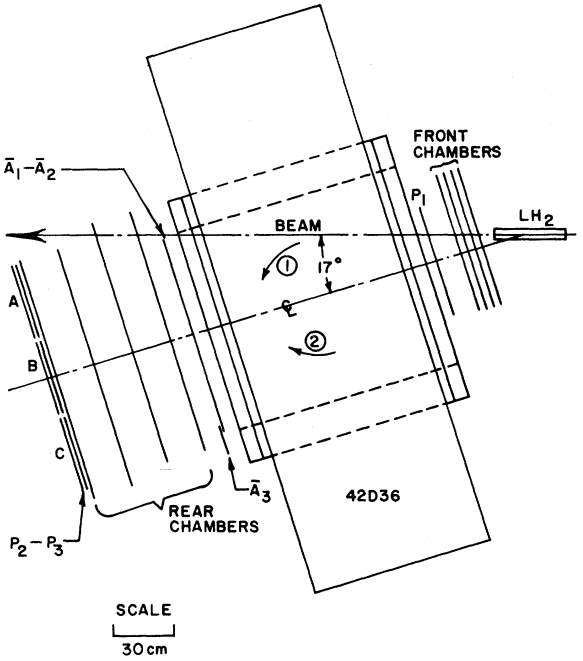

FIG. 2. Plan view of the wire-spark-chamber spectrometer in the narrow-angle configuration. Numbered arrows refer to the direction of bend of positive particles for a given data range.

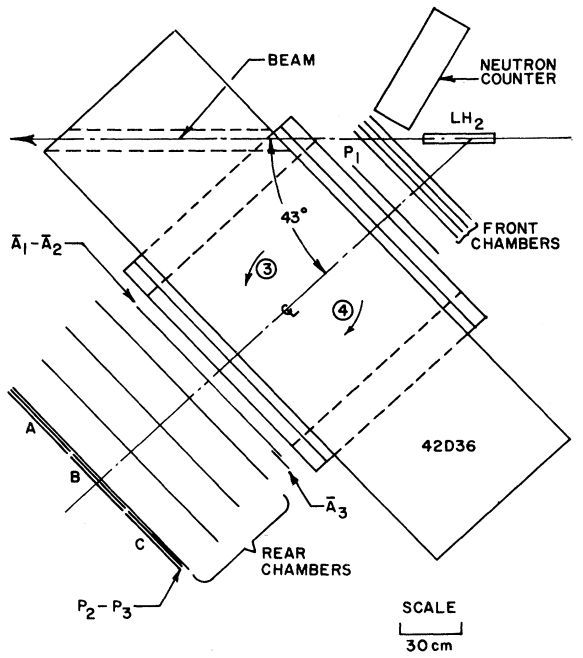

FIG. 3. Plan view of the spectrometer in the wide-angle configuration. The location of the neutron counter during its calibration is shown.

ter was 2.54 cm square. The third monitor was a three-counter telescope called π which was located in an unfocused positively charged beam taken from the first sweeping magnet in the beam (Fig. 1). The π telescope counters were made from 1.59-mm-thick scintillators, 2.54 cm square. They were spaced ~30 cm apart.

The BOT monitor was taken as a standard because of its high counting rate. A study of the observed ratios between the three monitors over the course of the experiment indicated that day-to-day fluctuations in the monitors were ~0.5%. This degree of monitor stability was entirely adequate for the experiment.

C. Time-of-flight techniques

The time origin of neutrons in the incident beam was determined to modulo ~67 nsec by placing a Čerenkov counter called T_0 near the production target of the synchrotron. The T_0 counter consisted of a radiator located ~60 cm from the production target, an air light pipe 1.2 m long, and a 56 AVP phototube. The radiator was a Lucite shell $11.4\times10.2\times5.1$ cm^3 filled with glycerin. One side was beveled for 6.4 cm along the 11.4-cm direction to permit Čerenkov light to escape into the air light pipe. The counter responded to charged particles with β greater than ~0.7.

Both the anode and dynode signals from one of the phototubes of T_0 were used. It was necessary to clip both the input and output signals in order to ensure an efficient response from the discriminators because of the high repetition rate of the input signals. The T_0 anode signal was attenuated by a factor of 2 and put in coincidence with a signal derived from the rf program of the accelerator. The output signal from this coincidence (T_{0L}) was largely free from tube noise and spurious signals not related to the on-target timing of the proton bunches in the synchrotron. The T_0 dynode signal (T_{02D}) was inverted and put in coincidence with T_{0L}. The timing of the output of this coincidence was that of T_{02D}, whose fast-rising leading edge was not impaired by attenuation. The signal then was passed through a variable delay in order to provide a means of correcting any timing drifts in the T_0 signal. The system produced a noise-free, stable, on-target timing signal.

In order to monitor and correct any possible drifts in the T_0 signal, a balance system or time vernier was set up. Using the π monitor, coincidences between the T_0 pulse and each of two pulses from the π telescope were made near the 50% efficiency point on opposite ends of the delay curve. The sensitivity of the balance system was better than 0.1 nsec. Adjustments of the delay were rarely necessary, and were less than 0.2 nsec.

The π telescope was also used to integrate the contamination from the internal proton bunches which were supposed to be empty. The ABC (alternate bunch contamination) scheme was based on the fact that all the charged particles in the beam have almost identical velocities. Two coincidences were set up: one with T_0 and signals from particles from the "right" proton bunch (ABC_A); the other with T_0 and particles from the "wrong" proton bunch (ABC_B). The ratio of the two coincidence rates ABC_B/ABC_A measured the contamination.

The T_0 tube voltage was plateaued with respect to both efficiency and resolution. The efficiency using the B monitor was measured to be ~95% by determining if a T_0 signal from the appropriate on-target proton bunch was present when a γ or neutron in the beam was detected in the B telescope. The resolution was checked using a Čerenkov counter consisting of a 56 AVP phototube with a 5-cm cylinder of Lucite fastened to its face, which was located in the beam ~25 m from the internal target. Using the γ's in the beam, a resolution of 1.32 nsec full width at half maximum (FWHM) was attained. The phototube on T_0 was run at 1900 V. Above this voltage the efficiency increased very little, but the resolution became worse. No deterioration in the performance of the counter was observed over the course of the experiment.

The efficiency of T_0 varied by ~5% depending on the beam conditions. In order to eliminate this variable efficiency as a source of error in the experiment the detection apparatus as well as the monitors were gated off for ~67 nsec whenever T_0 was missing. The various monitor counts as well as the number of neutral interactions were recorded both with and without the T_0 gate. Consequently, a number of independent checks of the T_0 efficiency were available throughout the experiment.

A scintillation counter called P_1 was used with T_0 to measure the flight time of the incident neutron (Figs. 2 and 3). This counter, which was part of the trigger logic for the proton spectrometer, responded to protons recoiling from n-p interactions in the LH_2 target. A correction was made in the analysis for the travel time of the recoiling proton. P_1 consisted of a scintillator 61 cm long horizontally $\times$15 cm long vertically and 0.32 cm thick. Light from the scintillator was fed to a 56 AVP phototube by 12 Lucite strips which were all the same length in order to make the counter as nearly isochronous as possible.

An extensive series of tests were made on P_1; it had good efficiency over its entire area and was isochronous to better than 0.1 nsec for all

particles intersecting a horizontal line contained in the plane of the scintillator. A slight correction was made in the analysis for particles striking the counter above or below the median of the magnet.

The time circuitry was adapted from a previous experiment performed at the PPA.[29] During the experiment two separate time-to-height converters (THC) were used in parallel. The input selectors were coincidence circuits operated on singles. This feature gave us the ability to select timing signals from a number of different telescopes. One system drove an analog-to-digital converter (ADC) whose output was placed in the core memory of the PDP-7 computer and subsequently written on magnetic tape. It was used primarily in conjunction with timing signals from P_1. A similar system was used to drive a 512-channel pulse-height analyzer. It served, among other things, as a useful check on the first system.

During the running of the experiment the T_0-P_1 TOF system was calibrated using γ's in the incident beam. A converter was placed in front of the LH_2 target and the spectrometer was turned off. The digitized position of the γ peak was observed. The time scale of the electronics was measured by moving the γ peak a known distance in time using a set of standard cables whose delay times were accurately known. The width of the γ timing peak was 2 nsec FWHM and we adopted this as our resolution. The linearity of the system was checked by driving it with pulses with random timing. It was found that the ADC was slightly nonlinear, and a correction was generated and used in the analysis of the data.

D. Wire-spark-chamber spectrometer

The scattering angles and momenta of recoiling charged particles from n-p interactions in the LH_2 target were determined using a magnetic spectrometer (Figs. 2 and 3). The spectrometer consisted of the following components: (a) a dipole magnet 1.07 m wide $\times$0.91 m deep with a 25.4-cm gap; (b) a set of wire spark chambers, with four gaps separated by 3.94 cm, placed in front of the magnet; (c) another set of wire chambers, with four gaps separated by 20.3 cm, located behind the magnet; and (d) a set of scintillation counters to define the spectrometer trigger and solid angle.

The spectrometer magnet was operated at a central field value of ~7.5 kG. The field integral along the center line in the median plane was 8.20 ± .08 kG m. The magnet was mapped in the median plane and a plane 8.9 cm above the median plane. The maximum grid spacing was 10.16 cm in the uniform central region, and the minimum grid spacing was 2.54 cm in the fringe-field region. Checks were made on the field symmetry above and below the median plane and no significant asymmetry was found. The field measurements were made using a Ge Hall probe which was calibrated with a nuclear magnetic resonance (NMR) probe. The field measurements were accurate to ~0.2%.

During the data-taking the magnetic field was set using the NMR probe, and the field setting was continuously monitored with a digital voltmeter placed across a 1-ohm resistance in the magnet current supply. Frequent checks of the field setting were made using the NMR probe. The stability of regulation was better than 0.1% over the course of the experiment.

It was necessary to shield the magnetostrictive delay lines in the wire chambers from the magnetic field. A 5-cm-thick iron shield was placed between the magnet and the front chambers and 1.9 cm of shielding behind the magnet. This reduced the magnetic fields in the vicinity of the delay lines to less than 50 G. The effect of the remaining field on the delay lines was tolerable.

The front chambers were constructed using fiberglass-epoxy (G-10) frames. Each gap had an active area 76.2 cm wide and 25.4 cm vertically and consisted of orthogonal wire planes epoxied to opposite sides of the G-10 frame and separated by 0.95 cm. The wires were spaced 1.06 mm apart. The first and last gaps had wires running horizontally and vertically, while in the middle two gaps the wires were oriented at 45° and 135°. The rear spark chambers were of a similar construction but larger. They had an active area 1.27 m wide and 0.41 m vertically. The wire orientation in the first and fourth chambers was 0° and 90° as in the front. In the middle two gaps, however, the wire orientation was 30° and 120° with respect to the horizontal. The gas volume of each gap was separate. Mylar windows 0.05 mm thick were fastened to the G-10 frames with RTV (silicon rubber cement). The chambers were operated with He gas.

In each gap one wire plane was connected to high voltage and the other to ground. The chambers were pulsed using a set of spark gaps and capacitors supplied commercially by Science Accessories Corporation. A clearing field of 20 volts was applied to the gaps. The high voltage system for the gaps was designed to drive the gaps 20 pulses/sec. Nevertheless, it was found that instantaneous rates above 3 pulses/sec resulted in a marked drop in chamber efficiency. It was established that the charging time for the pulsing system was not a limiting factor, but the effect itself was not understood. During the data-taking, the system was gated off for ~330 msec after each event.

The fact that each gap consisted of orthogonal wire planes resulted in long rise times for the high voltage and nonuniform efficiencies over the active areas of the chambers. In the front where the active area was small and the wires short, no nonuniformity of chamber efficiency was detected. However, in the rear chambers the effect was serious. The high voltage was applied to the shortest wires in each chamber, which improved the situation considerably, but up to ~10 cm on one side of each diagonal chamber was essentially dead.

The chamber readout system used magnetostrictive delay lines. They consisted of a Remendur ribbon 0.13×0.051 mm^2 in cross section attached to an aluminum wand. A current-sensitive amplifier connected to a pickup coil at one end of the delay line served to convert the magnetostrictive pulses into electrical signals. The techniques associated with the magnetostrictive readout of wire chambers have been discussed by previous authors.[30-32]

A set of three anticoincidence counters, $\bar{A}_1$, $\bar{A}_2$, and $\bar{A}_3$, surrounding the exit of the magnet on three sides were used to define partially the solid angle of the spectrometer and to help eliminate particles scattering from the poles of the magnet. One side was left open in order not to interfere with the incident neutron beam which passed through the spectrometer in one of the data-taking configurations. The three A counters were located 20.6 cm back of the rear pole face of the spectrometer. $\bar{A}_1$ and $\bar{A}_2$ were 1.07 m long and defined a 22.9-cm vertical aperture for the spectrometer. $\bar{A}_3$ placed a horizontal limitation on the spectrometer aperture on the side away from the beam 5 cm in from the magnet coils. Immediately behind the last rear chamber were located two sets of three counters (one set behind the other) which covered the active area of the last chamber. The first set was called P_{2A}, P_{2B}, P_{2C}; and the second set, P_{3A}, P_{3B}, P_{3C}. Defining the OR of $\bar{A}_1$, $\bar{A}_2$, $\bar{A}_3$ as $\bar{A}$, the following signatures were valid: $T_0 P_1 \bar{A} P_{2A} P_{3A}$, $T_0 P_1 \bar{A} P_{2B} P_{3B}$, $T_0 P_1 \bar{A} P_{2C} P_{3C}$. Any one was used to trigger the spark gaps from the chambers and the electronic readout system for the magnetostrictive delay lines and to gate off the fast logic for the duration of the readout cycle (Fig. 4).

E. Data-taking

Data were taken in four different angular ranges with the spectrometer magnet in two different physical configurations (see Table I). For each

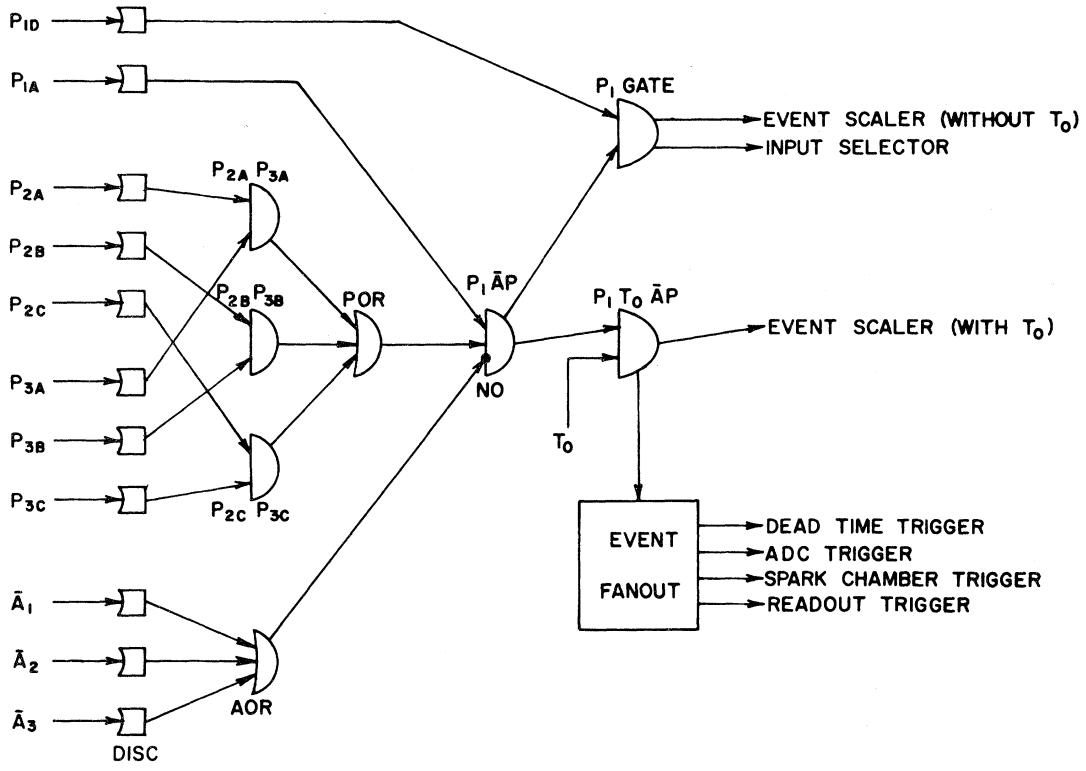

FIG. 4. Block diagram of the event trigger logic. The logic is described in detail in the text.

physical position of the magnet, the magnet was operated in both polarities. The direction of bend for positive-charged particles for the different angular ranges is indicated by numbered curved arrows in Figs. 2 and 3. Each angular range covered ~15° in the laboratory.

Each run consisted of a target-empty data set followed by a target-full data set. A target-full run consisted of about 40 000 triggers, approximately enough data to fill a 732-m magnetic tape. The target-empty running varied with the angular range but was typically ~2% of target-full triggers. Because of the greatly reduced event rate in range 4, the runs in this range were reduced to $\frac{1}{2}$ the number of triggers in ranges 1–3.

Before and after every run the PDP-7 computer was used to record the experimental conditions. Each scattering event was processed and written on magnetic tape in blocks of 20 events.[33] Scalers which recorded monitor counts for each run were recorded by hand at the end of the run. "Feedback" information from the on-line analysis was displayed on an oscilloscope and photographed frequently.

23 TOF calibration runs using converted γ's were made over the course of the experiment at intervals of from 1 to 3 days. Other calibration data included a set of four runs interspersed through the data-taking in which the spectrometer magnet was turned off. These straight-line track data served as a check on the spark-chamber alignment. Some data were taken in range 1 with the target empty and the sweeping magnets off; thus the momentum of incident beam protons could be determined both by TOF and by the spectrometer which served as a consistency check on the calibration of the spectrometer and the TOF system.

During much of the data-taking in ranges 1 and 2 there was another experiment in the neutral beam in front of the defining collimator at 21.3 m. This experiment had counters and a LH_2 target in the beam which was operated both full and empty during our data-taking. With the target full there was ~3.0 g/cm^2 of material in the beam, with the LH_2 accounting for ~0.7 g/cm^2 of the material. This experiment was removed from the beam prior to data-taking in ranges 3 and 4 and a vacuum pipe installed in its place. During the data-taking in range 3, a 1.9-cm CH_2 converter was placed in the B monitor. Range 4 was the only range during which no changes in the beam were made. Since it was also the configuration in which the incident neutron spectrum was measured, it was adopted as a standard. A set of momentum-dependent corrections to the measured cross sections was calculated and applied to the results. These corrections were always less than 5.1%.

TABLE I. Neutron-proton scattering data taken in this experiment.

Range	Approximate angular range	Number of runs	Triggers	Elastic events (600 MeV/c–2000 MeV/c)
1	0°–15.5°	17	613 620	197 429
2	15.5°–31°	12	388 480	141 417
3	31°–46.5°	11	388 820	124 847
4	46.5°–62°	5	67 100	39 247

F. Determination of the incident neutron spectrum

An absolute normalization of the measurements was achieved directly from the experiment using a neutron detector of known efficiency to measure the incident neutron spectrum by TOF. The efficiency of the detector was determined during the data-taking in ranges 3 and 4 by detecting scattered neutrons in coincidence with the proton spectrometer (Fig. 3). Since elastic events were kinematically determined *without* the neutron counter, we had a set of tagged neutrons.

The neutron detector consisted of a layered structure of scintillator and polyethylene, and was operated by demanding a coincidence between any two adjacent scintillators (Fig. 5). This detector required that a neutron produce a charged particle with enough energy to go through at least 5 cm of polyethylene. This was accomplished by guiding the light from alternate scintillators to common phototubes and requiring a coincidence between the output pulses of the two tubes. This design was chosen to make the momentum threshold for neutron detection about 0.5 GeV/c since our experiment covered a range of laboratory neutron momenta between 0.6 and 2.0 GeV/c. Approximately 1300 neutrons were detected in range 3 and ~2300 in range 4.

The incident neutron spectrum was measured by

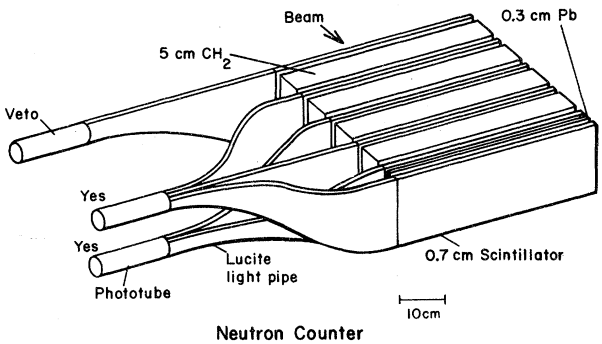

FIG. 5. The neutron detector used to determine the incident neutron flux.

placing the detector in the incident beam immediately in front of the LH_2 target. Although the synchrotron was operated with proton bunches separated by 134 nsec, there were still timing ambiguities. In order to unfold these ambiguities a spectrum was also taken 15.5 m from the Pt target.

The incident neutron spectrum was measured with the incident beam centered and normal to the detector face; but the tagged neutrons struck it over a wide range of its surface area and at various angles. Therefore, to understand the geometrical variations in efficiency a number of incident neutron spectra were taken with the beam striking the detector at various points and angles. The analysis of the data taken with this neutron detector and the results for the incident neutron spectrum will be presented in Sec. III G.

III. DATA ANALYSIS

The data for the reaction $n+p \to n+p$ are embedded in a larger class of data for the process $n+p \to X+Y$, where Y is a positively charged particle (usually a proton) whose three-momentum is measured with the spectrometer and X represents the other particle(s) (usually a neutron) in the final state. The data analysis consists of the following steps:

(1) The spectrometer data are used to reconstruct the three-momentum of the recoiling charged particle (particle Y).

(2) The TOF data on the incident neutron are used to determine its energy.

(3) The invariant mass of system X is calculated assuming that Y is a proton.

(4) The data are cut to select events for which X is equal to the neutron mass. This is the criterion for an elastic n-p scatter.

(5) The elastic data are binned and relative differential cross sections calculated.

(6) Corrections are made for resolution effects, indistinguishable backgrounds such as $np \to d\pi^0$, and other systematic effects.

(7) Finally, the incident neutron spectrum is used to yield absolute differential cross sections.

In connection with step (3) above it is important to note that in comparison with most reactions, an elastically scattered proton has the maximum possible momentum which can result from an n-p interaction for a given scattering angle and incident neutron energy. If Y is not a proton arising from an n-p scatter but some other particle, then the "missing mass" calculation of step (3) will yield a value for the invariant mass of X which is always larger than the mass of the neutron. The exceptions are the reactions $np \to d\pi^0$ and $np \to d\gamma$.[34] Of these two reactions only the first is important. Since the deuteron is heavier than the proton, if we detect a deuteron in the spectrometer and call it a proton, the calculated missing mass Y will for some kinematic regions overlap with the neutron mass. This background is discussed in Sec. III C.

A. Kinematical reconstruction of the spectrometer data

Referring to Fig. 6(a), we define a vertical plane normal to the incident beam passing through the center of the LH_2 target. The object of the analysis was to determine the five quantities x_T, y_T, x'_T, y'_T, and p (T-parameters) and their error matrix in the target plane, where x_T and y_T are the intercepts of the scattered particle trajectory in the target plane; $x'_T = dx/dz\,|_{z=z_T}$ and $y'_T = dy/dz\,|_{z=z_T}$ are the slopes of the trajectory in the plan and elevation views, respectively; p is the momentum of the particle. The analysis was carried out in two stages. Stage 1 consisted of finding the best-fit straight-line tracks in the front and rear spark chambers independently. Stage 2 consisted of

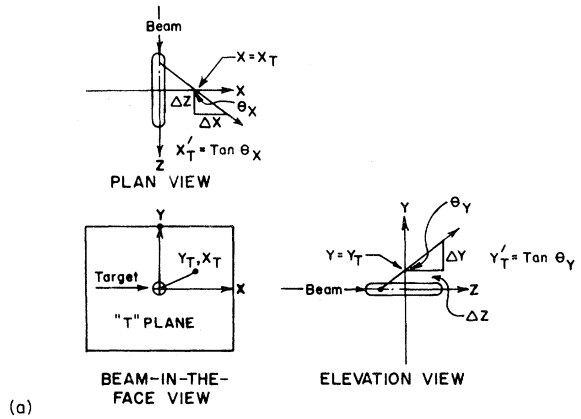

FIG. 6. (a) Definitions of the parameters used to characterize each scattered particle when it is projected back to the LH_2 target. (b) Notation used in the text to describe particle trajectories with respect to the spectrometer coordinate system.

fitting the quantities x_T, y_T, x'_T, y'_T, and p with the best-fit parameters from stage 1 used as input data by minimizing the statistical parameter χ^2 through an iterative procedure. The details are discussed below.

1. Straight-line track search

In order to look for straight-line tracks in the chambers it is necessary to transform the digitized spark information from the electronic readout system into a coordinate system common to all of the chambers. Using the surveyed location of the chambers and the "straight-line" data taken with the spectrometer magnet turned off, a consistent set of transformations was determined with spark locations in a common coordinate system. The velocity of sound in the delay lines was determined from the fiducial wires in each wire plane. Time-dependent drifts in the velocity of sound along the individual delay lines were corrected by recomputation after every 100 events. In identifying a straight-line track in either the front or the rear chambers the basic criterion was that at least 3 of the four gaps in each set of chambers had to produce sparks falling within a fixed distance of a straight line. In addition only one track in the front and rear chambers was allowed; otherwise, the event was rejected. A more detailed list of the steps taken in searching for tracks in the spark chambers is given in Ref. 31. Considerable care was taken in building the track-searching routines to ensure that "inefficiencies" were small. A check of several hundred events by hand indicated that the program gave doubtful results for less than 0.5% of the events.

For a successful event the output of the track-searching routines consisted of the fitted parameters for a straight-line track and an error matrix for both the front and rear chambers. In Fig. 6(b), we denote the fitted tracks in the front and rear chambers as F and R, respectively. The F and R tracks were parametrized in terms of four parameters, a slope and an intercept in the plan and elevation views. A total of eight parameters described the entrance and exit trajectories to the spectrometer magnet. A cut was made at a later stage in the analysis on the basis of the statistical parameter χ^2 for the F and R track fits.

2. Optimization of the spectrometer trajectory

Stage 2 involved fitting the four target parameters, x_T, y_T, x'_T, y'_T, and the particle momentum, p, to the F and R tracks by an iterative procedure. Since F and R are described by eight parameters, the fit has three degrees of freedom. We could fit the T-parameters directly to spark data. In this case there are a total of sixteen delay lines and five fitted parameters. Thus, there are eleven degrees of freedom. The advantage of using a two-stage fit with three degrees of freedom in the second stage is that χ^2 becomes a much more powerful statistic in eliminating "bad" events. In the single-stage case with eleven degrees of freedom, much of the power of the χ^2 statistic goes into "proving" that the spark data fall along a straight line. Since we test this independently in each chamber in stage 1 of the analysis, there is no point in weakening the χ^2 statistic in the second-stage analysis by redetermining information already established in stage 1 of the analysis.

The fit was patterned closely after a method developed by Boynton.[35] The method minimized χ^2, but proceeds by first linearizing the problem using first-order ray tracing methods in a bending magnet.[36] Because of the linearized character of the method, rapid convergence is assured only if the starting values of the T-parameters are sufficiently close to the optimal values. The starting value of the momentum is generated from the formula

$$p \propto \frac{\int \vec{B}\cdot d\vec{l}}{\sin\theta_1 + \sin\theta_2} , \tag{3.1}$$

where B is the magnetic field integrated along a straight line through the magnet, and θ_1 and θ_2 are the entrance and exit angles, respectively, in the plan view [see Fig. 6(b)]. A slight correction to this starting p value is made for the elevation angle of the trajectory in the magnetic field. The field integral is given by the expression

$$\int \vec{B}\cdot d\vec{l}\,(\text{kG m}) = 8.2278 + 0.1317\,[\tfrac{1}{2}(x_1+x_2)]^2 - 6.774\,[\tfrac{1}{2}(x_1+x_2)]^4 + 0.02159\,|\tfrac{1}{2}(z_1+z_2)| - 6.407\,(z_1-z_2)^2 , \tag{3.2}$$

where x_1 and x_2 are the horizontal entrance and exit coordinates of the particle trajectory; z_1 and z_2 are the vertical entrance and exit coordinates. The coordinate units are meters. A representative sample of data showed that the expression (3.2) was accurate to ~0.3% for 97% for the events on the basis of numerical integration of precise (0.1%) field map data. The remaining 3% were determined to ~0.6%. Starting values for the four remaining T-parameters were generated by projecting the

R track back through the magnet using a "square field" approximation and the starting value of p. Vertical focusing corrections were applied at the edges of the square field to correct for the fringing field of the magnet. Using these starting values for the T-parameters, a single "pass" through the fitting routines achieved a good fit. The χ_g^2 for the fit was later used as a basis for a cut in the data.

The method of analysis chosen was picked primarily because of its processing speed on a digital computer. In order to investigate possible systematic errors caused by the approximations in the computational method, a Monte Carlo program was written which generated a set of "exact" spectrometer trajectories by integration through the magnetic field. These exact trajectories were then used to check the accuracy of the faster computational methods used in the actual data analysis. They were also used to determine the expression for the field integral given in (3.2).

A comparison of 1000 "exact" events with the "approximate" results for the analysis program on the same events indicated that systematic errors introduced were negligible with respect to the inherent resolution of the spectrometer.

B. Corrections to the spectrometer data

1. *Ionization losses*

In terms of a "Plexiglas equivalent" the amount of material through which a recoiling proton passed before entering the spectrometer was ~0.834 g/cm^2. The amount of LH_2 in the path of the particle was computed independently for each event. Typically a proton traveled through ~0.3 g/cm^2, but in some cases the amount of hydrogen was as much as 2.5 g/cm^2. Corrections for these energy losses were made on the basis of tabulated values for the energy loss of protons in Plexiglas and hydrogen.[37]

2. *Geometrical efficiency*

For a point target, and fixed values of the incident momentum and polar scattering angle, the geometrical efficiency of the spectrometer is defined as

$$E_g = \frac{\phi_r}{2\pi} , \tag{3.3}$$

where ϕ_r is the azimuthal angular range over which the spectrometer can detect events. In the case of an extended target an appropriate average over the target volume must be included. In binning the data each event is corrected for scattering events which the spectrometer cannot "see" by the factor $1/E_g$.

The geometrical efficiency was determined from the data itself, and by a Monte Carlo program. Figure 7 shows the geometrical efficiency of the spectrometer for an incident momentum of 1000 MeV/c over the four ranges in which data were taken. In ranges 2, 3, and 4 the geometrical efficiency curves are relatively flat with steeply falling edges. The sharp edges are due to the horizontal limits of the spectrometer, and the flat portion is caused by the vertical aperture limits. In range 1 the spectrometer does not limit the solid angle from 0° to 3°. Starting at 3° the curve drops drastically. In order to limit any systematic effects from this behavior the data were cut for events in the range $-\frac{1}{2}\pi \leq \phi \leq \frac{1}{2}\pi$. In other words the geometrical efficiency is constrained to be $\leq 50\%$ starting at 3°. The more slowly varying behavior of the resulting curve eliminates the possibility of serious systematic error. The data were cut to eliminate the effects of the horizontal limits of the spectrometer. These cuts are indicated by arrows in Fig. 7. The angular location

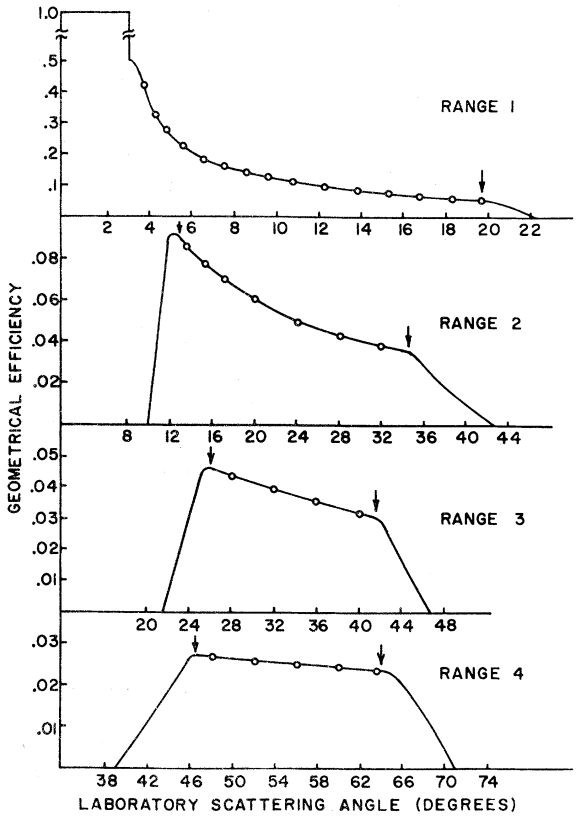

FIG. 7. Geometrical efficiency of the spectrometer for an incident momentum of 1000 MeV/c over the four ranges in which data were taken. In range 1 the spectrometer does not limit the solid angle from 0° to 3°. The arrows indicate cuts to eliminate the effects of the horizontal limits of the spectrometer. The circles were obtained directly from the data.

of these cuts as a function of the incident neutron momentum is shown in Fig. 8.

Over the angular ranges from which data were used the geometrical efficiency was determined to an accuracy of ~1%. It is possible to check this result by a direct comparison with the data. Figure 7 also shows this comparison at an incident momentum of 1000 MeV/c.[38] The results indicate that there are no systematic errors in the Monte Carlo result to an accuracy of ~1%.

An estimate of the error correlation coefficient introduced by this solid-angle correction between adjacent points in the angular distribution or between adjacent energy ranges is <10%.

Additional small corrections were made for the two spaces (~2.5 mm) between the three counters at the end of the spectrometer. The effect of each of these spaces was to deplete the number of events in a single angular bin for any given incident neutron energy. The magnitude was easily calculated, and the corrections ($\lesssim$ 10%) brought the affected points into line with the rest of the data.

3. *Chamber efficiencies*

The large active area of the rear chambers coupled with the intrinsic electrical properties of crossed-wire planes resulted in a nonuniform efficiency over the active area of the diagonal rear chambers. Corrections were generated to compensate for this effect on the basis of a comparison of 3-spark and 4-spark events in both front and rear chambers.

The method consisted of subdividing each chamber into a set of 2.5-cm squares and each delay line into 2.5-cm segments. For each chamber square and delay-line segment an efficiency was calculated using the data which survived the track-finding routine in the analysis program. The set of efficiencies was tabulated and used to weight each event according to the particular set of chamber squares through which the particle passed. The overall efficiency was greater than 98% for more than 90% of the events used. The few differential cross sections whose final value was corrected by more than 25% because of chamber efficiency were discarded.

C. Elastic selection criteria and inelastic backgrounds

The elastic selection criteria consisted of demanding that the reaction $n+p \rightarrow X+p$ have the invariant mass of X equal the neutron mass. Figure 9 shows a mass plot for X based on data taken from range 3 and averaged over the incident neutron spectrum. The mass resolution averaged over incident momentum is 30 MeV FWHM. The other ranges were similar.

The procedure for selecting elastic events and resolving the TOF ambiguity involved the following steps:

(1) Each event was assumed to be elastic, and

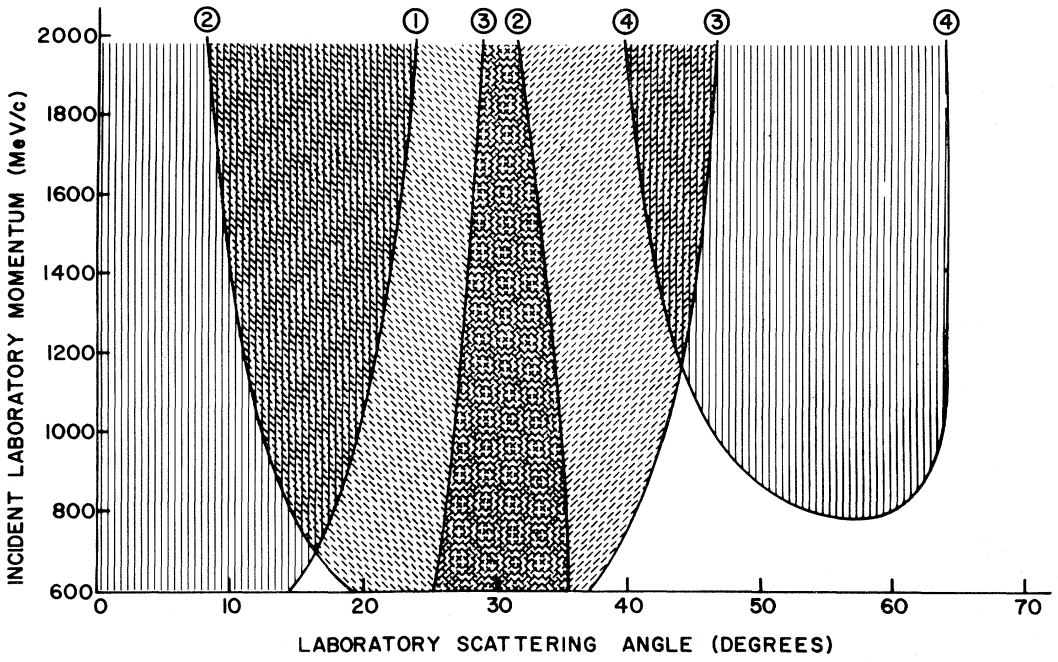

FIG. 8. Angular limits of acceptable elastic scattering data as a function of momentum.

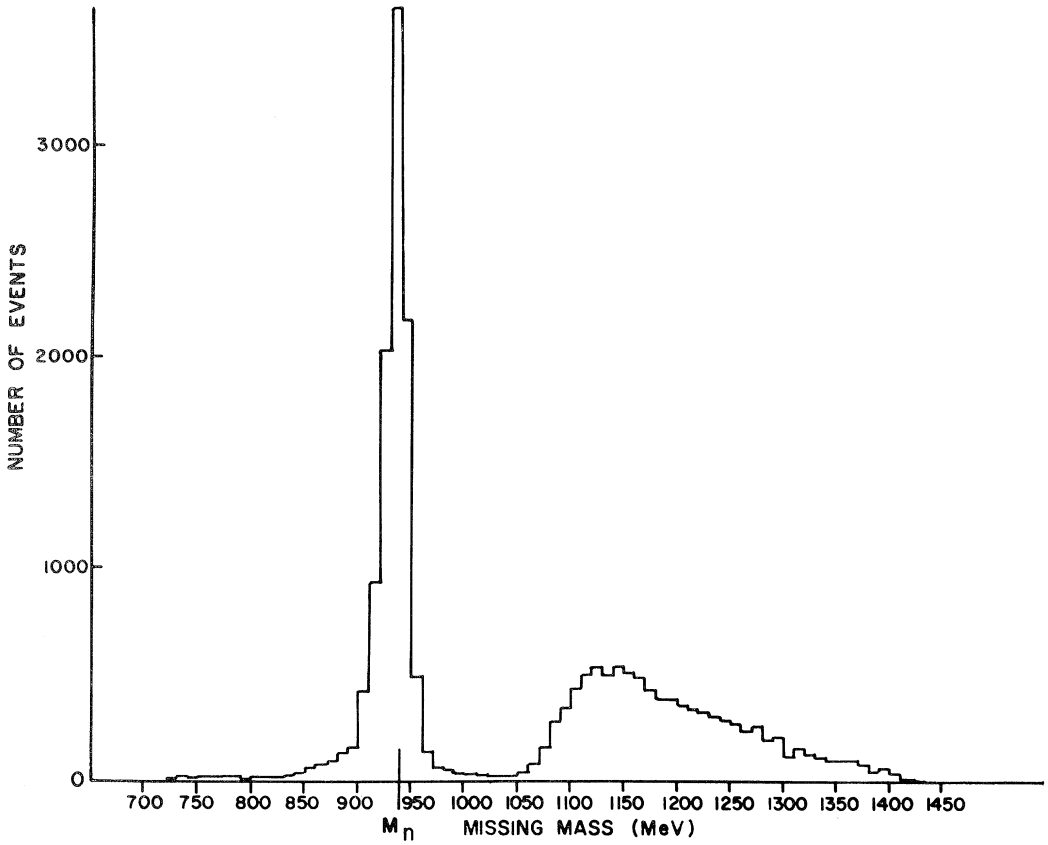

FIG. 9. Mass plot for the missing neutral system summed over the data from range 3. The elastic peak at the neutron mass (M_n) and inelastic production are visible.

the TOF of the incident neutron was calculated using the momentum and scattering angle of the recoiling proton.

(2) The difference between the TOF calculated in step 1 and the measured TOF was histogrammed as a function of incident momentum and laboratory scattering angle.

(3) If the difference computed in step 2 was greater than 33 nsec, 67.32 nsec were added to the measured TOF and step 2 repeated. The incident momentum label for each event was based on the measured TOF.

For elastic events the difference computed in step 2 peaks at zero. Inelastic scatters will yield a time difference greater than zero. High-energy inelastic scattering, which is interpreted as low-energy data, results in both positive and negative time differences. Elastic events were chosen by placing a window on the time-difference peak centered at zero. The window size was adjusted depending on the incident neutron momentum and varied between ±10 nsec at 600 MeV/c and ±6 nsec at 2000 MeV/c.

The advantages of these time-difference plots over the missing-mass plot as a basis for choosing elastic events are twofold. First, the time difference is closely related to one of the directly measured quantities in the experiment. Consequently, it is more convenient in resolving the ~67 nsec time ambiguity. Second, it was found to be easier to analyze and subtract the effects of inelastic scattering backgrounds. Examples of these time-difference plots at 687 MeV/c and 1485 MeV/c are shown in Fig. 10.

Three-body inelastic scattering backgrounds were of two kinds. The first was an inelastic contamination of high-energy elastic scattering data resulting from decreasing resolution at high energies [Fig. 10(a)]. This effect depended on both the incident energy and the laboratory scattering angle but was most serious in the forward direction, where it varied from nothing at 1200 MeV/c to 6% at 2000 MeV/c. The second inelastic contaminant of the data occurred only at low energies, where 67.32 nsec were added to the TOF. It arose from the ambiguity involved in distinguishing high-energy inelastic scattering from low-energy elastic scattering [Fig. 10(b)]. It was most serious

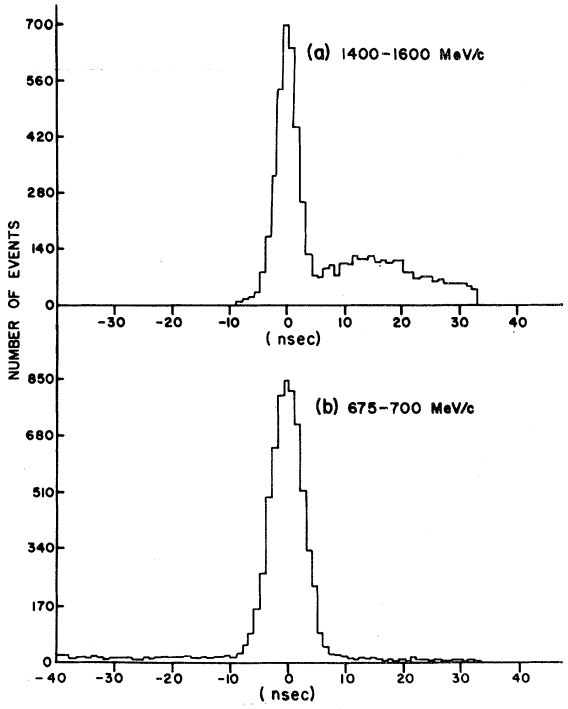

FIG. 10. Time-difference plots for two momentum intervals.

in the forward direction where the subtraction varied from 7% at 600 MeV/c to nothing at 760 MeV/c. The data between 760 and 1200 MeV/c were not affected by either type of background.

Special attention was given to the process $n+p \rightarrow d+\pi^0$. If the deuteron from this reaction is misinterpreted as a proton, it can simulate exactly elastic np scattering in our measurements at a series of energies and angles, e.g., 0° at 808 MeV/c, 5° at 1000 MeV/c. Heavier ionization energy losses and multiple Coulomb scattering broaden the TOF resolution for this process and diminish its effects.

Figure 11 shows TOF plots from the data (left side of the figure) which display the effect of this background. The peak at large values of ΔT which moves toward the elastic peak with increasing angle is due to deuterons produced backwards in the np c.m. system. The forward deuterons produce a peak which lies under the elastic peak and can be removed only by a Monte Carlo simulation of the process.

The quality of the simulation can be judged by comparing the simulated results (right-hand side of Fig. 11) to the corresponding data. The satellite peaks agree in position for the first three angular bins shown and then disappear from both samples in the bin for $\theta = 12-14°$ as the scattering angle exceeds the kinematic limit for $np \rightarrow d\pi^0$.

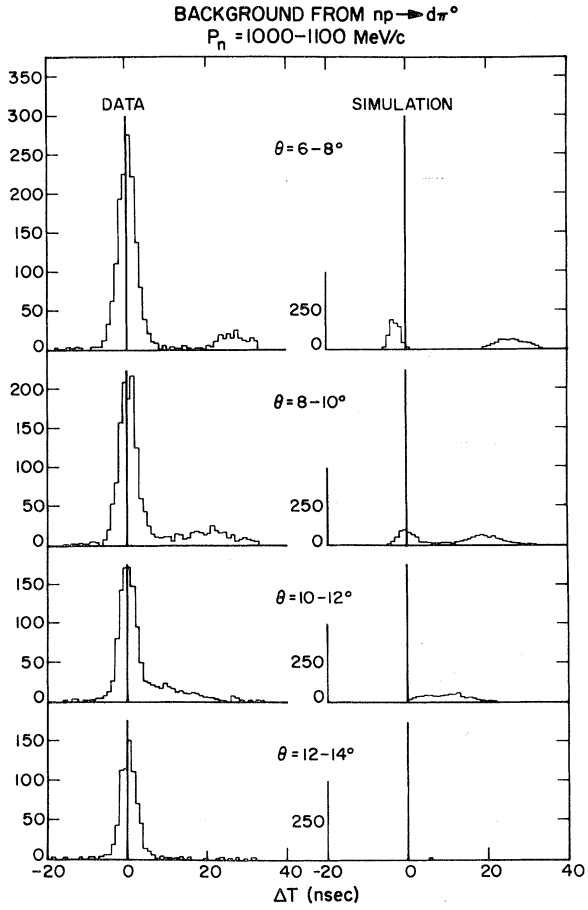

FIG. 11. Comparison of data (left-hand side of figure) and Monte Carlo simulation (right-hand side of figure) showing time-difference plots for selected angular intervals for incident momenta between 1000 and 1100 MeV/c. The satellite peak at positive ΔT due to the process $np \rightarrow d\pi^0$ is clearly visible.

Only a limited range of angles was affected at each energy. The magnitude of the correction varied from 3% in the forward direction at 0.8 GeV/c to 20% for lab angles of 15° at 1.7 GeV/c.

D. Miscellaneous cuts to the data

Two types of cuts were made based on the kinematically reconstructed data from the spectrometer:

(1) three χ^2 cuts on the fits for straight lines (χ^2_F and χ^2_R) and the trajectory (χ^2_t), and

(2) geometric cuts at the target and in the plane of the anticoincidence counters at the exit of the spectrometer.

The χ^2 cuts on the spectrometer data, χ^2_F and χ^2_R, were adjusted to cut 1% of the data. Estimates of physical processes such as nuclear scattering of recoiling protons in the spectrometer and scat-

tering of incident neutrons in the spectrometer structure indicated that they were a negligible contribution to the 1% of data removed by each of the cuts χ_F^2 and χ_R^2. It was concluded that a bad χ_F^2 or χ_R^2 was not correlated with physical processes which should be treated as "bad" data, but rather was associated with multiple Coulomb scattering in the front and rear chambers, mistakes in the track-searching routines, or a poor chamber response to a completely good event. Therefore, a correction was included in the final results for the data removed by the cuts.

A strong correlation between a "bad" χ_g^2 and events which scattered from the pole faces of the spectrometer was observed. This cut was adjusted so that the number of "good" events excluded by the cut were approximately equal to the number of "bad" events included by the cut. This cut also removed ~1% of the data. Since the cut was made in a self-compensating manner, no corrections in the final results were made for its effects.

In ranges 2, 3, and 4, cuts on the longitudinal and vertical target intersections of the spectrometer particle were made. These cuts eliminated events caused by neutron interactions in the LH_2 flask walls and target assembly (see target-empty background below). In range 1 these target cuts were not made because of the indeterminancy involved in computing the target intersection at very forward angles.

The cut on the vertical intersection of the spectrometer exit trajectory was consistent with the parameters used to define the exit aperture in the Monte Carlo program which determined the spectrometer solid angle.

E. Target-empty background

The target-empty data in the experiment were analyzed using the same target cuts described above in connection with the target-full running. In ranges 2, 3, and 4 the target-empty scattering was 0.8% of the target-full scattering. This is consistent with scattering from residual hydrogen gas at a temperature of ~60°K. Consequently, target-empty corrections were ignored in ranges 2, 3, and 4. In range 1 there were no target cuts and the target-empty scattering was ~2% of the target-full scattering. An investigation of the target-empty angular distribution indicated it was not significantly different from target-full. A flat 1.2% subtraction was made for target-empty effects in range 1.

F. Relative normalization of the different angular ranges

One of our most serious problems in the analysis was the relative normalization of the different angular ranges. The raw data show very little evidence of any systematic discrepancies between ranges for incident momenta below 1000 MeV/c representing over 70% of our data. Above 1000 MeV/c, ranges 2 and 4 seem systematically lower than ranges 1 and 3 by an amount which increases monotonically with incident neutron momentum to about a 40% discrepancy above 1600 MeV/c. The effect correlates with magnetic field direction.

When this effect was noticed, a thorough overhaul of the analysis procedure was made in an attempt to find the cause of the error.

All these studies strongly indicated the trouble was inefficiency in the triggering system, specifically a gain change in P_1 related to field direction. That counter had been studied extensively under field-free conditions and in position with the field direction of range 1. The counter was designed to eliminate any effects due to the position at which a particle passed through the scintillator. Voltage plateaus taken with a charged beam passing through a number of different positions showed no shift of the voltage plateaus with position. However, the counter was not replateaued with the field direction of ranges 2 and 4. The results of this error were not discovered until long after the apparatus was dismantled and the phototube on P_1 used elsewhere.

The inefficiency was clearly correlated with ionization energy loss of the proton in P_1, i.e., the amount of light. Using this information and the measured voltage plateaus, we developed a correction procedure for ranges 2 and 4 in terms of a single parameter—an effective reduction of voltage in the phototube. The corrected data of ranges 2 and 4 joined rather smoothly with ranges 1 and 3. All affected momenta gave approximately the same results for the voltage reduction, between 310 and 375 volts.

An arbitrary decision to renormalize ranges 2 and 4 to agree with ranges 1 and 3 would have yielded results close to the above procedure but would have neglected variations in dE/dx as a function of angle for a fixed incident neutron energy. The maximum variation of this effect within a range is 15% for range 2 at 1045 MeV/c. The validity of the procedure is strongly supported by the fact that an identical effect was observed in a measurement of pp elastic scattering with the same apparatus.[39] In that experiment the data of range 1 agrees with independent experiments. Reference 8 describes all these matters in greater detail.

In making the corrections described above, the correction which reconciled ranges 1 and 2 usually made all ranges consistent. The exceptions were at 784 MeV/c and at the highest three momenta,

where range 3 seemed consistently above ranges 2 and 4 by 10% to 35%. These four momenta are the ones most sensitive to small errors in the TOF system. The high momenta are affected because both the beam intensity and the cross section are very sensitive functions of TOF. The momentum bin at 784 MeV/c is affected because it brackets the "wrap-around" point in the TOF spectrum which arises from the 67.32 nsec timing ambiguity. A slight error in timing, well within the given time bin, can cause an apparent normalization error. In this case, a timing error of 0.8 nsec was sufficient to explain the inconsistencies observed without producing any significant effect in the rest of the data. The appropriate corrections were made to range 3 at the affected momenta. However, the existence of this effect at one magnet configuration suggests an uncertainty in the normalization of the overall angular distribution, since range 3 might be the correct result, and the other three ranges could be in error. Therefore, we have added (in quadrature) $\frac{1}{2}$ the range-3 correction to the overall systematic uncertainty at the affected momenta. The factor-of-2 reduction comes from the square root of the number of ranges.

G. Incident beam normalization

The neutron counter used to obtain the absolute normalization of the data was discussed in detail in Sec. II F.

During the data-taking in ranges 3 and 4 the neutron counter was positioned to cover the kinematic "shadow" of the proton spectrometer for elastic n-p scatters. For an elastic event the neutron momentum and trajectory were determined from the proton trajectory and intersection with the LH_2 target. If the computed neutron trajectory passed through the full thickness of the counter, a check was made to see if it had been detected. The efficiency of the counter for a given neutron momentum interval equals the number detected at that momentum divided by the number which passed through the counter. This provided us with a calibrated detector for measuring the incident beam flux.

During the beam flux measurement the neutron beam passed through the center of the counter normal to its face. During the n-p scattering experiment, neutrons passed through the counter over the greater part of its area and at various angles with respect to the normal. In order to understand the differences in detection efficiency in the two circumstances, a number of geometrical studies were made on the counter. It was placed in the incident beam and its response as a function of neutron energy was measured with the neutron beam passing through the counter at a number of different points and angles. Differences between efficiencies for the beam flux measurement and the calibration data were computed, but they depended on unverified assumptions about the falloff of efficiency near the edge of the counter. This was the method used in the widely quoted but unpublished report in Ref. 8.

To check these assumptions, a Monte Carlo program was written to study the neutron counter. It accounted for the incident beam properties, scattering in hydrogen, the geometric acceptance of the spectrometer, and the location of the neutron counter. It produced a sample of elastic scattering events statistically identical, in all measurable respects, with the experimental sample used for the calibration. Neutrons from these events were traced through a Monte Carlo model of the detector. The neutron and any interaction products were followed until they left the counter. This model gave a number and distribution of detected neutrons which agreed with the experimental sample up to 1.2 GeV/c, where pion production became important and was not well simulated by the model.

The program was also run to simulate the measurements with the neutron counter in the direct beam. By comparing this result with the Monte Carlo determined efficiency of the neutron counter for detecting neutrons at each incident momentum with neutrons distributed over the counter a correction (<10%) was determined and applied to the experimental calibration sample. No correction was required below 800 MeV/c and the correction was extrapolated to the region above 1.2 GeV/c where the absolute efficiency determined by the Monte Carlo was no longer reliable. Figure 12 shows a plot of the neutron-counter efficiency determined in this way. A smooth curve was drawn through the data points. The error corridor was determined from the functional fit described in Ref. 8. These efficiencies were used to determine the incident neutron spectrum required to calculate the absolute differential cross sections.

IV. PRESENTATION OF THE DATA AND CONCLUSIONS

A. Results for the n-p differential cross sections

The results for the elastic n-p differential cross sections are given in Table II. The same results are presented graphically in Fig. 13. Each entry presents data averaged over an interval of incident neutron momentum. The choice of intervals was made to correspond to bins of ~4 nsec in the TOF

of the incident neutrons. Within each energy interval the data were binned typically in intervals of two degrees in the laboratory polar scattering angle. Average values for $|t|$ and $\cos\theta_{\text{c.m.}}$ were computed for each angular bin. The incident energy was averaged over the entire angular distribution.

The tabulated errors for the cross sections arise from three sources: counting statistics (which dominate the errors), the uncertainty in the correction for the geometrical efficiency of the spectrometer, and the uncertainty in the correction for chamber efficiency. These are statistically independent for any single point. The geometrical efficiency corrections introduce only small correlations ($\lesssim$10%) between points and correlations arising from chamber efficiency corrections were found to be negligible.

The overall normalization uncertainty, presented separately with the data in each energy bin, is dominated by the uncertainty in the detection efficiency of the neutron counter. It is based on the error corridor in Fig. 12. A more conservative estimate of the error can be made using the data points in Fig. 12. Apart from the normalization error given in the tables, there is an overall systematic error of ~2% in the normalization resulting from an unexplained shift in monitor ratios between data-taking for the differential cross sections and the measurement of the incident neutron spectrum.

The final values for the differential cross sections differ somewhat from those which have been widely circulated.[8,40] The changes result from the following corrections:

(1) reanalysis of the malfunction of counter P_1;

(2) inclusion of corrections due to the cracks between scintillation counters P_{2i}, P_{3i} and P_{2j}, P_{3j};

(3) recomputation of the background subtraction taking into account the influence of $np \to d\pi^0$;

(4) recomputation of the incident neutron spectrum; and

(5) correction for assumed TOF errors in range 3.

The bulk of the data are unaffected by changes (1)–(3), isolated points have been altered by up to 20%. Item (4) resulted in normalization changes up to 10% at some energies. Item (5) affected range 3 relative to ranges 2 and 4 at four momenta.

A major feature of our data which has already been reported[7] concerns the energy dependence of the sharp peaking near $|u|=0$. Using our reanalyzed data the results presented in Ref. 7 have been recalculated. No significant differences from the earlier results have been found.

In addition to this peaking our data show other features of the n-p interaction. For slightly larger momentum transfers [$|u|>0.02$ (GeV/c)^2] the cross section falls off with a slope characteristic of diffraction peaks [$\propto e^{bt}$, with $b \sim 10$ (GeV/c)$^{-2}$]. The cross sections reach a minimum near but not at 90°, and they are definitely not symmetric about 90°.

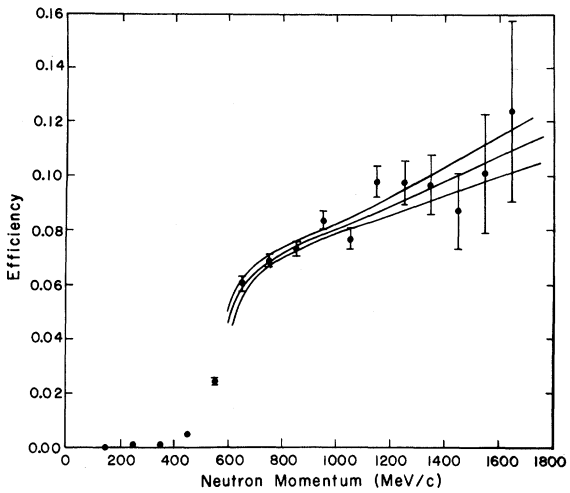

FIG. 12. Absolute efficiency of the neutron detector as a function of momentum. The data points were obtained from the calibration using elastic events. A smooth curve was drawn and the error corridor was calculated in Ref. 8.

B. Comparison with other experiments

Our data are in qualitative agreement[23] with the previous experiments[41-50] in our momentum range. There are quantitative discrepancies which may be characterized as of two types. (1) Our data tend to show steeper peaking at small momentum transfers. This may be due to the improved resolution of our experiment. (2) There is a discrepancy of ~25% between the normalization of our experiment and older data between 640 and 840 MeV/c.[24]

A review of experiments[42-50] in the same momentum range as ours is given below. No clear resolution of the normalization difference has been reached. We have not been able to rule out the possibility that our results should be revised upward by about 25%. However, no justification can be found within the experiment for such a renormalization.

In Table III the principal features of these experiments are summarized and we comment on comparisons with our data at similar energies. With the exception of the cloud-chamber experiment,[44] these experiments are similar in technique. All use a quasimonoenergetic neutron beam produced by charge exchange of a proton beam. Data were often taken with different target and detector configurations over several angular

TABLE II. Neutron-proton elastic differential cross sections.

P (MeV/c)	T (MeV)	$-u$ [(GeV/c)^2]	$d\sigma/du$ [mb/(GeV/c)^2]	θ (deg)	$\cos\theta$	$d\sigma/d\Omega$ (mb/sr)	Systematic uncertainty (%)
612 (600–625)	182	0.000 05	319.9 ± 17.1	178.6	−0.9997	8.67 ± 0.46	8.0
		0.000 28	322.5 ± 12.0	176.8	−0.9984	8.76 ± 0.32	
		0.000 74	305.4 ± 8.9	174.7	−0.9957	8.30 ± 0.24	
		0.001 42	297.9 ± 15.0	172.6	−0.9917	8.09 ± 0.41	
		0.002 33	285.3 ± 10.2	170.5	−0.9864	7.75 ± 0.28	
		0.003 45	253.8 ± 9.8	168.5	−0.9798	6.89 ± 0.27	
		0.005 53	219.4 ± 6.6	165.4	−0.9676	5.95 ± 0.18	
		0.009 11	211.4 ± 6.8	161.2	−0.9466	5.74 ± 0.19	
		0.047 48	125.9 ± 4.1	136.2	−0.7215	3.42 ± 0.11	
		0.056 35	113.6 ± 4.0	132.1	−0.6703	3.09 ± 0.11	
		0.065 68	104.7 ± 3.8	127.9	−0.6147	2.84 ± 0.10	
		0.075 60	94.1 ± 2.2	123.9	−0.5573	2.56 ± 0.06	
		0.085 99	86.4 ± 2.2	119.8	−0.4964	2.35 ± 0.06	
		0.096 80	78.9 ± 2.0	115.6	−0.4328	2.14 ± 0.06	
637 (625–650)	196	0.000 06	362.6 ± 20.7	178.6	−0.9997	10.62 ± 0.61	5.5
		0.000 31	342.0 ± 11.9	176.7	−0.9983	10.00 ± 0.35	
		0.000 79	316.4 ± 9.1	174.7	−0.9957	9.25 ± 0.27	
		0.001 54	289.7 ± 14.7	172.6	−0.9916	8.47 ± 0.43	
		0.002 54	254.5 ± 9.8	170.5	−0.9862	7.42 ± 0.28	
		0.003 74	248.3 ± 9.9	168.4	−0.9797	7.26 ± 0.29	
		0.005 98	211.5 ± 6.6	165.3	−0.9674	6.18 ± 0.19	
		0.009 93	211.8 ± 6.8	161.1	−0.9459	6.19 ± 0.20	
		0.042 68	122.4 ± 4.2	140.1	−0.7676	3.58 ± 0.12	
		0.051 40	119.1 ± 4.1	136.1	−0.7203	3.48 ± 0.12	
		0.060 76	110.1 ± 3.9	132.0	−0.6688	3.21 ± 0.12	
		0.071 10	99.2 ± 3.7	127.8	−0.6134	2.90 ± 0.11	
		0.081 76	86.9 ± 2.2	123.7	−0.5545	2.54 ± 0.06	
		0.093 06	79.2 ± 2.1	119.6	−0.4933	2.32 ± 0.06	
		0.104 70	77.7 ± 2.1	115.5	−0.4300	2.28 ± 0.06	
		0.116 70	65.1 ± 2.6	111.4	−0.3641	1.90 ± 0.07	
662 (650–675)	210	0.000 06	350.2 ± 20.8	178.6	−0.9997	10.96 ± 0.65	3.6
		0.000 33	308.3 ± 10.9	176.7	−0.9983	9.65 ± 0.34	
		0.000 86	308.7 ± 9.0	174.6	−0.9956	9.68 ± 0.28	
		0.001 65	285.4 ± 14.3	172.6	−0.9916	8.95 ± 0.46	
		0.002 72	269.4 ± 10.1	170.5	−0.9862	8.44 ± 0.31	
		0.004 05	238.3 ± 9.6	168.4	−0.9794	7.47 ± 0.30	
		0.006 53	210.9 ± 6.5	165.2	−0.9668	6.61 ± 0.20	
		0.010 71	195.5 ± 6.5	161.0	−0.9457	6.13 ± 0.20	
		0.045 92	121.2 ± 4.1	140.1	−0.7669	3.80 ± 0.13	
		0.055 54	113.3 ± 3.9	135.9	−0.7179	3.55 ± 0.13	
		0.065 67	104.7 ± 3.8	131.8	−0.6668	3.29 ± 0.12	
		0.076 90	94.0 ± 3.6	127.6	−0.6098	2.95 ± 0.11	
		0.088 17	79.3 ± 2.1	123.5	−0.5521	2.49 ± 0.07	
		0.100 20	72.3 ± 2.0	119.4	−0.4910	2.27 ± 0.06	
		0.112 80	69.6 ± 1.9	115.3	−0.4271	2.18 ± 0.06	
		0.125 70	57.4 ± 2.3	111.2	−0.3612	1.80 ± 0.07	
687 (675–700)	224	0.000 07	325.2 ± 19.5	178.6	−0.9997	10.91 ± 0.65	3.2
		0.000 36	292.3 ± 10.5	176.7	−0.9983	9.79 ± 0.35	
		0.000 92	276.2 ± 8.2	174.6	−0.9956	9.26 ± 0.27	
		0.001 77	253.0 ± 13.0	172.6	−0.9916	8.47 ± 0.44	
		0.002 92	254.2 ± 9.5	170.4	−0.9861	8.51 ± 0.32	
		0.004 32	217.0 ± 9.0	168.4	−0.9795	7.27 ± 0.30	
		0.006 99	200.1 ± 6.2	165.2	−0.9668	6.71 ± 0.21	
		0.011 46	166.0 ± 5.8	161.0	−0.9456	5.56 ± 0.20	
		0.049 40	105.4 ± 3.8	139.9	−0.7653	3.53 ± 0.13	
		0.059 55	101.8 ± 3.8	135.8	−0.7172	3.41 ± 0.13	

TABLE II *(Continued)*

P (MeV/c)	T (MeV)	$-u$ [(GeV/c)^2]	$d\sigma/du$ [mb/(GeV/c)^2]	θ (deg)	$\cos\theta$	$d\sigma/d\Omega$ (mb/sr)	Systematic uncertainty (%)
		0.070 82	98.3 ± 3.7	131.6	−0.6636	3.30 ± 0.12	
		0.082 40	78.5 ± 3.3	127.5	−0.6088	2.63 ± 0.11	
		0.094 75	67.3 ± 1.8	123.4	−0.5499	2.25 ± 0.06	
		0.107 70	62.9 ± 1.8	119.2	−0.4883	2.11 ± 0.06	
		0.121 10	59.8 ± 1.8	115.2	−0.4252	2.01 ± 0.06	
		0.135 00	50.2 ± 2.1	111.1	−0.3592	1.69 ± 0.07	
712 (700–725)	239	0.000 08	268.7 ± 16.4	178.6	−0.9997	9.61 ± 0.59	3.1
		0.000 38	279.3 ± 10.1	176.7	−0.9983	9.99 ± 0.36	
		0.000 99	257.0 ± 7.8	174.6	−0.9956	9.19 ± 0.28	
		0.001 93	232.5 ± 12.0	172.5	−0.9914	8.31 ± 0.43	
		0.003 14	225.6 ± 8.9	170.4	−0.9860	8.07 ± 0.32	
		0.004 68	190.0 ± 8.4	168.3	−0.9791	6.79 ± 0.30	
		0.007 55	183.0 ± 6.0	165.1	−0.9664	6.55 ± 0.21	
		0.012 38	152.7 ± 5.5	160.9	−0.9449	5.46 ± 0.20	
		0.018 23	143.5 ± 5.6	156.7	−0.9187	5.12 ± 0.20	
		0.042 89	104.1 ± 3.7	144.0	−0.8090	3.72 ± 0.13	
		0.053 23	89.5 ± 3.4	139.7	−0.7631	3.20 ± 0.12	
		0.064 01	91.5 ± 3.4	135.6	−0.7147	3.27 ± 0.13	
		0.075 89	75.8 ± 3.2	131.4	−0.6619	2.71 ± 0.11	
		0.088 43	72.1 ± 3.1	127.3	−0.6063	2.58 ± 0.11	
		0.101 60	64.2 ± 1.8	123.2	−0.5477	2.30 ± 0.06	
		0.115 50	58.3 ± 1.8	119.0	−0.4852	2.08 ± 0.06	
		0.129 80	54.7 ± 1.7	115.0	−0.4219	1.96 ± 0.06	
		0.144 50	48.2 ± 2.0	110.9	−0.3564	1.72 ± 0.07	
741 (725–760)	257	0.000 08	304.5 ± 14.0	178.6	−0.9997	11.72 ± 0.54	3.0
		0.000 42	256.1 ± 8.7	176.7	−0.9983	9.85 ± 0.33	
		0.001 07	242.8 ± 6.6	174.6	−0.9956	9.34 ± 0.25	
		0.002 09	208.4 ± 10.3	172.4	−0.9913	8.02 ± 0.40	
		0.003 41	183.0 ± 6.8	170.4	−0.9859	7.04 ± 0.26	
		0.005 07	171.5 ± 6.8	168.2	−0.9790	6.60 ± 0.26	
		0.008 13	149.2 ± 4.5	165.1	−0.9663	5.74 ± 0.17	
		0.013 47	135.8 ± 4.3	160.8	−0.9442	5.22 ± 0.17	
		0.019 96	124.3 ± 4.3	156.5	−0.9174	4.78 ± 0.17	
		0.046 43	91.1 ± 3.0	143.9	−0.8079	3.51 ± 0.12	
		0.057 43	83.2 ± 2.8	139.7	−0.7623	3.20 ± 0.11	
		0.069 26	77.0 ± 2.7	135.5	−0.7134	2.96 ± 0.11	
		0.082 29	62.3 ± 2.4	131.3	−0.6598	2.40 ± 0.09	
		0.095 75	61.3 ± 2.4	127.1	−0.6035	2.36 ± 0.09	
		0.110 00	56.4 ± 1.5	123.0	−0.5449	2.17 ± 0.06	
		0.124 80	51.5 ± 1.4	118.9	−0.4833	1.98 ± 0.06	
		0.140 80	46.6 ± 1.3	114.7	−0.4177	1.79 ± 0.05	
		0.156 40	40.8 ± 1.5	110.7	−0.3527	1.57 ± 0.06	
		0.173 20	37.2 ± 1.5	106.5	−0.2842	1.43 ± 0.06	
784 (760–810)	284	0.000 09	241.5 ± 10.7	178.6	−0.9997	10.24 ± 0.45	8.0
		0.000 47	208.3 ± 6.5	176.6	−0.9982	8.85 ± 0.28	
		0.001 20	198.2 ± 5.3	174.6	−0.9955	8.43 ± 0.22	
		0.002 32	192.7 ± 8.9	172.4	−0.9913	8.20 ± 0.38	
		0.003 84	154.6 ± 5.4	170.3	−0.9856	6.56 ± 0.23	
		0.005 63	137.7 ± 5.1	168.2	−0.9789	5.84 ± 0.22	
		0.009 10	126.5 ± 3.5	165.0	−0.9658	5.37 ± 0.15	
		0.015 07	110.1 ± 3.3	160.6	−0.9435	4.68 ± 0.14	
		0.022 27	100.9 ± 3.3	156.4	−0.9165	4.29 ± 0.14	
		0.052 25	73.5 ± 2.5	143.6	−0.8045	3.13 ± 0.10	
		0.064 07	65.5 ± 2.2	139.4	−0.7597	2.78 ± 0.09	
		0.077 27	60.3 ± 2.1	135.3	−0.7104	2.57 ± 0.09	
		0.091 55	51.3 ± 2.0	131.1	−0.6568	2.18 ± 0.08	

TABLE II *(Continued)*

P (MeV/c)	T (MeV)	$-u$ [(GeV/c)^2]	$d\sigma/du$ [mb/(GeV/c)^2]	θ (deg)	$\cos\theta$	$d\sigma/d\Omega$ (mb/sr)	Systematic uncertainty (%)
		0.106 60	47.9± 1.9	126.9	−0.6003	2.04 ± 0.08	
		0.122 50	41.4± 1.0	122.7	−0.5400	1.76 ± 0.04	
		0.139 00	36.3± 0.9	118.6	−0.4781	1.54 ± 0.04	
		0.156 00	34.3± 0.9	114.4	−0.4136	1.45 ± 0.04	
		0.174 10	32.7± 1.0	110.3	−0.3466	1.38 ± 0.04	
		0.191 80	30.2± 1.1	106.2	−0.2787	1.28 ± 0.05	
829 (810–850)	313	0.000 10	217.3 ± 11.2	178.6	−0.9997	10.18 ± 0.52	2.4
		0.000 52	213.0± 7.3	176.6	−0.9982	9.98 ± 0.34	
		0.001 34	197.7± 6.4	174.5	−0.9954	9.26 ± 0.30	
		0.002 60	174.9± 8.9	172.4	−0.9912	8.18 ± 0.41	
		0.004 25	132.5± 5.9	170.3	−0.9856	6.21 ± 0.28	
		0.006 29	116.5± 5.6	168.1	−0.9786	5.45 ± 0.26	
		0.010 18	116.6± 3.8	164.9	−0.9654	5.46 ± 0.18	
		0.016 84	110.9± 3.8	160.5	−0.9428	5.20 ± 0.18	
		0.025 02	96.1± 3.5	156.2	−0.9149	4.50 ± 0.17	
		0.058 18	71.4± 2.5	143.3	−0.8021	3.34 ± 0.12	
		0.071 68	56.4± 2.2	139.2	−0.7567	2.64 ± 0.10	
		0.085 98	53.6± 2.2	135.0	−0.7071	2.51 ± 0.10	
		0.101 80	46.8± 2.0	130.8	−0.6533	2.19 ± 0.09	
		0.118 90	44.5± 2.0	126.6	−0.5960	2.08 ± 0.09	
		0.136 70	40.3± 1.1	122.3	−0.5349	1.88 ± 0.05	
		0.155 50	36.1± 1.1	118.2	−0.4718	1.70 ± 0.05	
		0.174 30	32.3± 1.1	114.0	−0.4071	1.51 ± 0.05	
		0.193 70	28.4± 1.2	109.9	−0.3402	1.32 ± 0.06	
		0.213 70	27.5± 1.3	105.8	−0.2726	1.29 ± 0.06	
874 (850–900)	344	0.000 12	210.4 ± 10.2	178.4	−0.9996	10.79 ± 0.52	2.1
		0.000 58	191.9± 6.6	176.6	−0.9982	9.85 ± 0.34	
		0.001 51	175.1± 5.7	174.4	−0.9953	8.99 ± 0.29	
		0.002 89	163.4± 8.2	172.3	−0.9910	8.39 ± 0.42	
		0.004 72	132.1± 5.4	170.2	−0.9854	6.79 ± 0.28	
		0.007 01	112.4± 4.8	168.0	−0.9783	5.77 ± 0.25	
		0.011 34	96.6± 3.3	164.8	−0.9648	4.96 ± 0.17	
		0.018 65	90.6± 3.1	160.4	−0.9422	4.65 ± 0.16	
		0.027 44	78.9± 2.9	156.2	−0.9149	4.05 ± 0.15	
		0.050 47	62.9± 2.2	147.5	−0.8435	3.23 ± 0.12	
		0.064 27	59.3± 2.2	143.2	−0.8008	3.04 ± 0.11	
		0.079 28	53.4± 2.1	138.9	−0.7534	2.73 ± 0.10	
		0.095 27	46.6± 1.9	134.7	−0.7039	2.38 ± 0.09	
		0.113 40	39.4± 1.7	130.4	−0.6482	2.02 ± 0.09	
		0.131 10	36.2± 1.6	126.3	−0.5921	1.86 ± 0.08	
		0.151 40	35.3± 1.0	122.0	−0.5305	1.81 ± 0.05	
		0.171 60	28.4± 1.1	117.8	−0.4668	1.46 ± 0.06	
		0.192 80	25.4± 1.0	113.7	−0.4019	1.31 ± 0.06	
		0.213 60	23.2± 1.0	109.6	−0.3359	1.20 ± 0.05	
		0.236 60	22.4± 1.0	105.4	−0.2653	1.15 ± 0.05	
		0.259 30	22.8± 1.1	101.3	−0.1960	1.17 ± 0.06	
923 (900–950)	378	0.000 13	190.9± 9.8	178.6	−0.9997	10.76 ± 0.55	2.0
		0.000 65	185.1± 6.8	176.6	−0.9982	10.45 ± 0.38	
		0.001 66	159.5± 5.5	174.4	−0.9953	9.01 ± 0.31	
		0.003 19	135.3± 7.3	172.3	−0.9910	7.64 ± 0.41	
		0.005 30	125.1± 5.7	170.1	−0.9851	7.07 ± 0.32	
		0.007 84	99.2± 4.7	167.9	−0.9779	5.61 ± 0.27	
		0.012 69	93.9± 3.6	164.6	−0.9643	5.31 ± 0.20	
		0.020 77	69.7± 2.9	160.3	−0.9415	3.94 ± 0.16	
		0.056 17	58.3± 2.2	147.3	−0.8411	3.27 ± 0.13	
		0.071 79	52.5± 2.1	142.9	−0.7975	2.97 ± 0.12	
		0.088 31	47.5± 2.0	138.7	−0.7508	2.68 ± 0.11	

TABLE II *(Continued)*

P (MeV/c)	T (MeV)	$-u$ [(GeV/c)^2]	$d\sigma/du$ [mb/(GeV/c)^2]	θ (deg)	$\cos\theta$	$d\sigma/d\Omega$ (mb/sr)	Systematic uncertainty (%)
		0.106 90	44.5± 2.0	134.3	−0.6985	2.51 ± 0.11	
		0.126 20	38.5± 1.8	130.2	−0.6449	2.17 ± 0.10	
		0.146 90	32.8± 1.7	125.8	−0.5847	1.85 ± 0.09	
		0.168 70	29.4± 0.9	121.6	−0.5247	1.66 ± 0.05	
		0.191 20	23.9± 1.0	117.4	−0.4604	1.35 ± 0.06	
		0.214 40	21.1± 1.0	113.3	−0.3948	1.19 ± 0.05	
		0.238 50	21.0± 1.0	109.1	−0.3274	1.18 ± 0.06	
		0.262 40	19.5± 1.0	105.1	−0.2603	1.10 ± 0.05	
		0.288 70	19.7± 1.0	100.8	−0.1866	1.12 ± 0.06	
		0.412 50	24.0± 1.2	80.8	0.1607	1.36 ± 0.07	
		0.436 50	26.4± 1.3	76.8	0.2289	1.49 ± 0.07	
		0.459 70	28.6± 1.3	72.8	0.2956	1.61 ± 0.08	
		0.482 40	30.0± 1.4	68.9	0.3598	1.70 ± 0.08	
		0.504 80	30.8± 1.5	65.1	0.4212	1.74 ± 0.08	
974 (950–1000)	414	0.000 14	178.2 ± 9.7	178.4	−0.9996	11.03 ± 0.60	2.0
		0.000 73	164.8 ± 6.4	176.5	−0.9981	10.18 ± 0.40	
		0.001 85	147.8 ± 5.4	174.4	−0.9953	9.14 ± 0.33	
		0.003 58	126.8 ± 6.7	172.2	−0.9908	7.84 ± 0.42	
		0.005 83	105.4 ± 5.1	170.1	−0.9850	6.51 ± 0.31	
		0.008 75	93.9 ± 4.9	167.8	−0.9775	5.80 ± 0.30	
		0.014 04	81.0 ± 3.4	164.6	−0.9639	5.01 ± 0.21	
		0.022 75	67.7 ± 3.0	160.3	−0.9415	4.18 ± 0.18	
		0.047 64	57.1 ± 2.3	151.3	−0.8772	3.53 ± 0.14	
		0.062 48	53.6 ± 2.2	147.0	−0.8390	3.31 ± 0.13	
		0.079 41	44.9 ± 1.9	142.7	−0.7955	2.78 ± 0.11	
		0.098 40	39.9 ± 1.8	138.3	−0.7468	2.47 ± 0.11	
		0.118 50	33.0 ± 1.7	134.0	−0.6949	2.04 ± 0.10	
		0.140 00	30.5 ± 1.6	129.8	−0.6398	1.89 ± 0.09	
		0.162 50	25.2 ± 1.4	125.5	−0.5806	1.55 ± 0.09	
		0.186 80	22.5 ± 0.8	121.2	−0.5185	1.39 ± 0.05	
		0.211 50	20.4 ± 0.9	117.1	−0.4550	1.26 ± 0.06	
		0.237 20	16.7 ± 0.9	112.9	−0.3891	1.03 ± 0.05	
		0.264 60	15.0 ± 0.8	108.6	−0.3196	0.93 ± 0.05	
		0.290 90	15.7 ± 0.9	104.5	−0.2500	0.97 ± 0.05	
		0.317 90	15.6 ± 0.9	100.4	−0.1803	0.97 ± 0.06	
		0.428 20	18.7 ± 1.0	84.2	0.1005	1.16 ± 0.07	
		0.453 90	22.0 ± 1.1	80.2	0.1694	1.36 ± 0.07	
		0.478 70	22.6 ± 1.2	76.3	0.2360	1.40 ± 0.08	
		0.504 40	27.0 ± 1.3	72.5	0.3002	1.66 ± 0.08	
		0.531 00	28.0 ± 1.4	68.5	0.3668	1.74 ± 0.09	
		0.553 30	27.7 ± 1.4	64.7	0.4271	1.71 ± 0.09	
		0.577 30	33.2 ± 1.6	60.9	0.4869	2.04 ± 0.10	
1045 (1000–1100)	466	0.000 17	146.4 ± 6.7	178.4	−0.9996	10.20 ± 0.47	2.4
		0.000 84	139.4 ± 4.9	176.5	−0.9981	9.71 ± 0.34	
		0.002 14	121.0 ± 4.6	174.3	−0.9951	8.43 ± 0.32	
		0.004 12	104.3 ± 5.4	172.1	−0.9906	7.27 ± 0.38	
		0.006 77	87.2 ± 4.0	169.9	−0.9846	6.08 ± 0.28	
		0.010 02	81.2 ± 3.8	167.7	−0.9771	5.64 ± 0.26	
		0.016 09	64.9 ± 2.7	164.4	−0.9631	4.51 ± 0.19	
		0.026 69	56.0 ± 2.4	159.9	−0.9389	3.90 ± 0.17	
		0.039 34	49.0 ± 2.0	155.5	−0.9103	3.42 ± 0.14	
		0.054 87	47.1 ± 1.7	151.0	−0.8746	3.28 ± 0.12	
		0.072 08	43.1 ± 1.5	146.6	−0.8348	2.99 ± 0.10	
		0.091 21	38.5 ± 1.5	142.3	−0.7912	2.68 ± 0.10	
		0.112 20	31.6 ± 1.3	138.0	−0.7428	2.18 ± 0.09	
		0.135 70	26.5 ± 1.1	133.6	−0.6893	1.84 ± 0.08	
		0.160 30	24.1 ± 1.1	129.3	−0.6329	1.67 ± 0.08	

TABLE II. *(Continued)*

P (MeV/c)	T (MeV)	$-u$ [(GeV/c)^2]	$d\sigma/du$ [mb/(GeV/c)^2]	θ (deg)	cosθ	$d\sigma/d\Omega$ (mb/sr)	Systematic uncertainty (%)
		0.186 20	18.7±0.9	125.0	−0.5738	1.30±0.07	
		0.213 50	17.1±0.5	120.8	−0.5113	1.18±0.04	
		0.242 20	15.7±0.6	116.5	−0.4458	1.09±0.04	
		0.270 70	12.5±0.5	112.3	−0.3795	0.87±0.04	
		0.302 30	12.1±0.5	108.0	−0.3083	0.84±0.04	
		0.331 60	11.2±0.5	103.9	−0.2403	0.77±0.04	
		0.363 40	12.3±0.6	99.8	−0.1700	0.85±0.04	
		0.485 00	16.6±0.7	83.7	0.1103	1.15±0.05	
		0.515 30	17.3±0.7	79.6	0.1798	1.20±0.05	
		0.544 30	20.0±0.8	75.8	0.2458	1.39±0.06	
		0.574 40	21.8±0.9	71.8	0.3120	1.51±0.06	
		0.603 60	23.4±0.9	67.9	0.3756	1.64±0.07	
		0.628 50	25.3±1.0	64.1	0.4361	1.77±0.07	
		0.655 30	29.5±1.1	60.3	0.4951	2.05±0.08	
		0.678 30	31.7±1.3	56.6	0.5512	2.20±0.09	
1145 (1100–1200)	542	0.000 20	122.9±6.4	178.4	−0.9996	9.97±0.52	3.1
		0.001 00	99.4±4.6	176.4	−0.9980	8.05±0.37	
		0.002 54	90.5±5.0	174.3	−0.9950	7.32±0.41	
		0.004 93	77.8±4.9	172.0	−0.9903	6.28±0.40	
		0.008 07	65.8±3.9	169.8	−0.9841	5.33±0.32	
		0.012 08	52.9±3.3	167.5	−0.9763	4.29±0.27	
		0.019 15	45.7±2.6	164.2	−0.9623	3.69±0.21	
		0.031 89	34.8±2.2	159.6	−0.9374	2.82±0.18	
		0.047 20	32.8±2.1	155.1	−0.9070	2.65±0.17	
		0.065 13	28.9±1.1	150.7	−0.8722	2.35±0.09	
		0.085 27	27.2±1.2	146.3	−0.8320	2.20±0.10	
		0.109 50	23.5±1.1	141.7	−0.7846	1.90±0.09	
		0.134 20	16.8±0.9	137.4	−0.7355	1.35±0.08	
		0.161 30	16.7±0.9	133.1	−0.6829	1.35±0.08	
		0.192 00	13.8±0.8	128.5	−0.6222	1.11±0.07	
		0.222 20	12.7±0.8	124.2	−0.5627	1.03±0.07	
		0.254 20	11.9±0.4	120.0	−0.4995	0.96±0.04	
		0.288 50	10.1±0.4	115.6	−0.4319	0.82±0.03	
		0.322 80	8.4±0.4	111.5	−0.3658	0.68±0.04	
		0.355 60	7.7±0.4	107.3	−0.2970	0.62±0.04	
		0.391 00	7.1±0.4	103.1	−0.2274	0.57±0.04	
		0.430 60	7.2±0.4	98.9	−0.1549	0.58±0.04	
		0.465 10	7.6±0.5	94.9	−0.0848	0.62±0.04	
		0.573 20	10.8±0.6	82.7	0.1264	0.87±0.05	
		0.606 50	12.3±0.6	78.8	0.1945	1.00±0.05	
		0.643 10	13.2±0.7	74.7	0.2632	1.08±0.06	
		0.675 70	15.7±0.8	71.0	0.3257	1.27±0.07	
		0.708 70	17.9±0.8	67.1	0.3896	1.45±0.07	
		0.738 10	19.9±0.9	63.3	0.4489	1.61±0.08	
		0.765 60	23.2±1.0	59.6	0.5055	1.87±0.09	
		0.798 50	25.8±1.2	55.6	0.5643	2.09±0.11	
		0.823 50	28.3±1.5	52.1	0.6149	2.30±0.12	
		0.848 90	31.7±1.8	48.4	0.6637	2.58±0.15	
1281 (1200–1400)	649	0.000 26	78.2±3.9	178.4	−0.9996	7.64±0.38	9.1
		0.001 24	69.2±3.3	176.4	−0.9980	6.74±0.32	
		0.003 24	53.2±3.0	174.1	−0.9947	5.17±0.30	
		0.006 25	46.8±2.9	171.8	−0.9898	4.56±0.28	
		0.010 17	43.9±2.6	169.5	−0.9834	4.28±0.25	
		0.015 21	34.6±2.1	167.2	−0.9752	3.37±0.20	
		0.024 40	28.3±1.6	163.8	−0.9601	2.74±0.15	
		0.039 73	25.1±1.4	159.2	−0.9348	2.43±0.14	

TABLE II. *(Continued)*

P (MeV/c)	T (MeV)	$-u$ [(GeV/c)^2]	$d\sigma/du$ [mb/(GeV/c)^2]	θ (deg)	$\cos\theta$	$d\sigma/d\Omega$ (mb/sr)	Systematic uncertainty (%)
		0.059 11	20.1±0.8	154.6	−0.9031	1.96±0.08	
		0.081 50	16.3±0.7	150.0	−0.8663	1.57±0.07	
		0.107 40	12.6±0.6	145.5	−0.8242	1.22±0.07	
		0.136 20	9.5±0.5	141.0	−0.7770	0.93±0.05	
		0.166 90	8.6±0.5	136.4	−0.7239	0.83±0.05	
		0.202 30	6.9±0.4	132.0	−0.6689	0.67±0.04	
		0.237 80	5.8±0.4	127.5	−0.6092	0.56±0.04	
		0.275 10	5.6±0.3	123.1	−0.5456	0.54±0.04	
		0.313 20	5.0±0.2	118.9	−0.4831	0.48±0.03	
		0.358 40	4.6±0.3	114.5	−0.4145	0.45±0.02	
		0.398 60	4.1±0.3	110.3	−0.3468	0.41±0.02	
		0.439 00	4.1±0.3	106.1	−0.2768	0.40±0.02	
		0.486 30	3.4±0.2	101.8	−0.2037	0.33±0.02	
		0.526 80	3.5±0.3	97.6	−0.1314	0.34±0.02	
		0.655 80	7.2±0.4	85.5	0.0782	0.69±0.04	
		0.696 10	8.0±0.4	81.4	0.1487	0.77±0.04	
		0.734 60	10.0±0.5	77.7	0.2134	0.95±0.05	
		0.773 70	11.4±0.6	73.7	0.2814	1.10±0.06	
		0.823 60	14.1±0.7	69.7	0.3466	1.38±0.07	
		0.860 80	17.3±0.8	65.9	0.4088	1.68±0.08	
		0.894 90	18.7±0.8	62.2	0.4663	1.82±0.09	
		0.930 10	24.1±1.1	58.4	0.5238	2.34±0.11	
		0.963 30	29.5±1.5	54.7	0.5784	2.87±0.15	
		0.997 10	34.1±2.1	50.9	0.6303	3.31±0.20	
1484 (1400–1600)	817	0.000 34	55.6±3.3	178.4	−0.9996	6.81±0.41	13.0
		0.001 63	48.4±2.4	176.3	−0.9979	5.94±0.29	
		0.004 33	42.6±2.1	173.9	−0.9944	5.23±0.25	
		0.008 36	38.3±1.9	171.5	−0.9891	4.69±0.23	
		0.013 74	33.5±1.7	169.2	−0.9822	4.13±0.20	
		0.020 28	28.7±1.5	166.8	−0.9736	3.50±0.19	
		0.032 50	20.2±0.9	163.3	−0.9579	2.49±0.12	
		0.053 60	16.6±0.8	158.5	−0.9303	2.02±0.10	
		0.078 79	13.4±0.5	153.8	−0.8972	1.64±0.06	
		0.108 80	10.6±0.4	149.1	−0.8581	1.29±0.05	
		0.143 30	9.0±0.5	144.4	−0.8128	1.09±0.07	
		0.180 50	6.6±0.5	139.8	−0.7634	0.79±0.06	
		0.223 20	5.9±0.4	135.1	−0.7085	0.73±0.06	
		0.264 80	3.9±0.4	130.8	−0.6532	0.46±0.04	
		0.313 10	4.1±0.4	126.1	−0.5892	0.49±0.05	
		0.372 60	3.3±0.4	121.4	−0.5211	0.39±0.04	
		0.419 60	2.7±0.4	117.0	−0.4538	0.32±0.04	
		0.470 50	2.5±0.2	112.9	−0.3889	0.31±0.02	
		0.521 90	2.1±0.2	108.5	−0.3171	0.26±0.02	
		0.583 60	2.0±0.2	104.1	−0.2429	0.24±0.02	
		0.636 20	1.8±0.2	100.0	−0.1733	0.21±0.02	
		0.679 10	1.8±0.2	95.9	−0.1027	0.20±0.02	
		0.743 50	1.8±0.2	91.7	−0.0302	0.21±0.02	
		0.798 60	1.9±0.2	87.6	0.0427	0.23±0.03	
		0.856 00	2.5±0.2	83.5	0.1138	0.30±0.03	
		0.904 90	2.8±0.2	79.6	0.1803	0.33±0.03	
		0.955 10	3.2±0.3	75.9	0.2443	0.39±0.04	
		1.009 00	4.9±0.3	71.8	0.3116	0.60±0.05	
		1.048 00	4.3±0.3	68.1	0.3735	0.53±0.04	
		1.098 00	6.6±0.4	64.2	0.4349	0.81±0.06	
		1.147 00	8.0±0.6	60.4	0.4937	0.99±0.07	
		1.179 00	10.7±0.7	56.9	0.5455	1.30±0.09	
		1.230 00	13.2±1.0	53.3	0.5983	1.62±0.13	
		1.268 00	16.7±1.7	49.6	0.6485	2.04±0.20	

TABLE II. *(Continued)*

P (MeV/c)	T (MeV)	$-u$ [(GeV/c)^2]	$d\sigma/du$ [mb/(GeV/c)^2]	θ (deg)	$\cos\theta$	$d\sigma/d\Omega$ (mb/sr)	Systematic uncertainty (%)
1729 (1600–2000)	1028	0.000 44	37.6±2.6	178.2	−0.9995	5.81±0.40	19.3
		0.002 30	38.8±2.1	176.0	−0.9976	6.01±0.32	
		0.005 90	32.6±1.4	173.7	−0.9939	5.00±0.22	
		0.011 40	25.8±1.2	171.2	−0.9883	3.99±0.19	
		0.018 63	24.2±1.2	168.7	−0.9807	3.74±0.19	
		0.027 84	18.2±1.0	166.3	−0.9715	2.83±0.16	
		0.044 06	14.4±0.7	162.7	−0.9548	2.24±0.11	
		0.072 24	10.9±0.6	157.7	−0.9252	1.66±0.09	
		0.107 00	8.6±0.3	152.8	−0.8891	1.32±0.05	
		0.147 20	6.3±0.3	147.9	−0.8471	0.95±0.05	
		0.192 20	5.8±0.4	143.1	−0.8000	0.88±0.07	
		0.246 20	3.8±0.3	138.3	−0.7467	0.58±0.04	
		0.298 50	3.4±0.3	133.6	−0.6897	0.53±0.05	
		0.358 20	2.8±0.3	129.0	−0.6289	0.43±0.05	
		0.431 80	2.2±0.3	123.8	−0.5569	0.35±0.04	
		0.482 60	1.8±0.3	119.9	−0.4980	0.28±0.04	
		0.558 70	1.6±0.3	115.2	−0.4265	0.26±0.04	
		0.614 30	1.3±0.1	111.1	−0.3594	0.19±0.02	
		0.693 80	1.0±0.1	106.5	−0.2836	0.16±0.02	
		0.769 80	1.0±0.1	101.9	−0.2064	0.15±0.02	
		0.830 80	0.8±0.1	98.1	−0.1403	0.12±0.02	
		0.891 60	0.6±0.1	93.9	−0.0677	0.11±0.01	
		1.047 00	0.9±0.1	85.4	0.0795	0.16±0.02	
		1.098 00	1.1±0.1	81.4	0.1487	0.18±0.03	
		1.163 00	1.6±0.2	77.6	0.2151	0.26±0.03	
		1.254 00	1.1±0.1	73.7	0.2803	0.18±0.03	
		1.293 00	1.7±0.2	69.8	0.3448	0.26±0.03	
		1.363 00	2.7±0.3	66.0	0.4060	0.42±0.04	
		1.400 00	3.8±0.3	62.5	0.4625	0.58±0.05	
		1.487 00	3.9±0.3	58.6	0.5217	0.60±0.06	
		1.517 00	6.0±0.5	55.0	0.5738	0.90±0.09	
		1.550 00	6.9±0.8	51.6	0.6207	1.05±0.13	
		1.624 00	8.9±1.0	48.0	0.6696	1.37±0.17	

ranges. For c.m. scattering angles between 30° and 180°, the differential cross section was determined by the number of recoil protons in a counter telescope. Range was used to reject protons resulting from low-energy beam neutrons and the thickness of the range material was varied as a function of scattering angle. Above the inelastic threshold, range and Čerenkov counters were used to reject pions and muons. Only the cloud chamber used magnetic analysis on the protons. All measurements near 180° involved putting the proton detector in or near the neutron beam downstream from the scattering target. In some cases, this might have affected the beam-intensity monitors which were located farther downstream in the beam.

We believe that our experiment has some obvious advantages: a single liquid hydrogen target, a single detector with magnetic analysis of the proton momentum, determination of the incident neutron energy for each event, and a one-constraint fit to each event for elasticity. Particularly important is the simultaneous measurement of a broad range of angles near 180° (forward protons). All other workers using electronic techniques necessarily modified the experimental environment as a function of proton angle.

Since we do not measure the differential cross section at all angles, we cannot normalize to the total elastic cross section as do most other experimenters. Such a procedure involves a separate experiment with a neutron detector at forward angles, the adjustment of relative normalization to reconcile the separate measurements in overlapping regions, and an overall normalization factor to make the area under the differential cross section curve agree with the total cross section. The region of overlap may be near the useful limit for each of the detector types. An error, e.g., in the angular dependence of the neutron detection

efficiency, could distort the entire curve in order to produce the correct total cross section. The value of the total cross section used in Ref. 44 is probably 5 mb low, but all other experimenters have adopted values we consider accurate.

In order to normalize our data, we chose to determine the absolute flux of the incident neutron beam as described in Sec. III G. Larsen,[49] using a somewhat different technique, was the only other worker to attempt this, and his normalization is only about one standard deviation different from ours.

The comparisons summarized in Table III are based largely on graphical comparisons. In some cases, we have also attempted to fit identical functions, except for a normalization factor, to the two data sets. The procedure was to fit a curve of the form

$$d\sigma/du = Ae^{\alpha u} + Be^{\beta u} + Ce^{\gamma t}$$

to our data and minimize χ^2 with respect to the parameters. Where only backward data were involved, the last term was dropped. The parameters were then fixed and a normalization factor was adjusted to minimize a χ^2 comparison with the other experiment. When very bad fits were found, the points at or near 180° were dropped and the fit was attempted again. Significant improvements were found. This certainly confirms the observations made in Ref. 24; the shapes of these curves are different, with our data showing a significantly sharper peaking near $u = 0$. No conclusions should be based on the absolute values of χ^2 mentioned here for two reasons. First, the fitting function itself has uncertainties not included in the last stage of the calculation. Second, there are correlations in the data themselves which have not been accounted for. For example, some data show discontinuities at the boundary between regions covered by different detectors. We have attempted here only to support our visual observations. In general data which seemed to agree reasonably well showed χ^2 per degree of freedom less than 2.0. Those with obvious poor agreement yielded values greater than 5.0.

C. Energy dependence of the cross sections

Graphs of the s dependence of the intercept and slope of the differential cross section at $u = 0$ were presented in Ref. 7. A paper by Londergan and Thaler[23] pointed out that the general features of this energy dependence which are evident from our data were already present in the n-p phase shift analysis. They showed that the structure is contained mostly in the spin-singlet amplitude, which indicates that the one-pion exchange is involved.

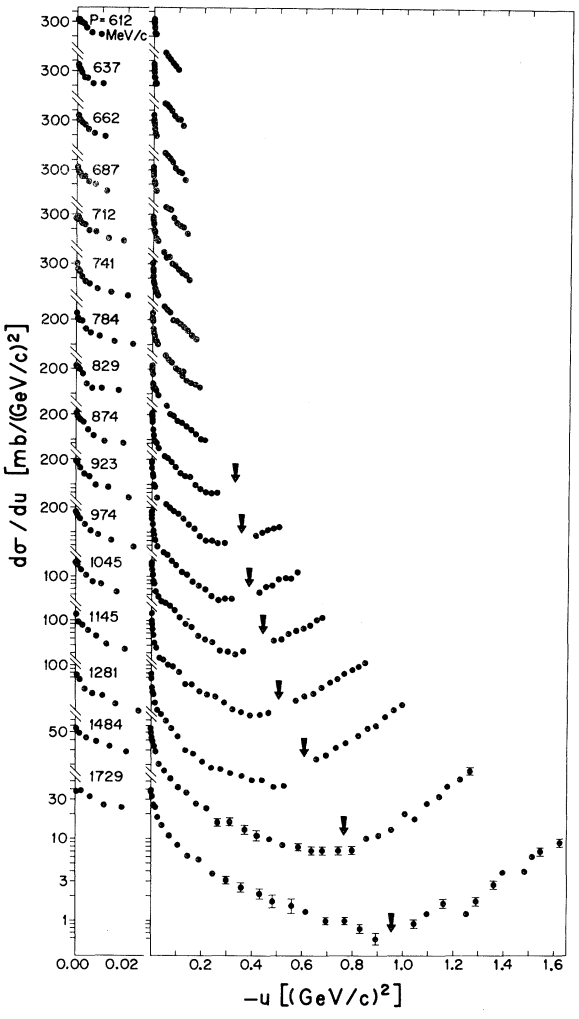

FIG. 13. n-p charge-exchange differential cross sections measured in this experiment. The arrows at the higher momenta indicate the position of 90° in the center-of-mass system. The quantity u is the square of the four-momentum transfer between the incident neutron and the outgoing proton.

In fact it has long been accepted that the existence of the peaking is due to an interference between the one-pion-exchange part of the amplitude and a "background" amplitude which is slowly varying in $|u|$. The exact nature of this background is not understood. Two models which produce satisfactory results at high energies differ in the details of the background amplitude. These are the droplet model[21] and the strong-cut Regge absorption model.[22]

Additional information can be obtained by examining the s dependence of quantities similar to the intercept with u fixed at other, nonzero, values. Data from other experiments have been included

TABLE III. Comparison with other experiments.

First author (Ref.)	Kinetic [a] energies (MeV)	Beam intensity monitor	Proton recoil data: Target (g/cm^2)	Proton recoil data: Detector [b] (angular resolution)	Scattered neutron data: Target (g/cm^2)	Scattered neutron data: Detector [b]	Number of data ranges	Normalized to agree with	Compared over (t) range $(GeV/c)^2$	Agreement (χ^2/DF): overall	Agreement (χ^2/DF): without forward points	Renormalization factor
Kazarinov (42)	200 (196)	unspecified	CH_2-C (3.0) CH_2-C (1.5) CH_2-C (0.5)	Range in Cu + scintillator (1°) and (2°)	CH_2-C (3.5) LH_2 (1.0)	Converter and scintillators (3°) and (2°)	5 targets 4 detectors	σ_{tot} = 42.7 mb	0–0.12	poor 83/10	good 16/8	1.32
Kelly (43)	260 (257)	Bi fission downstream	CH_2-C (?)	Range in W + proportional counters (3°) [c]			1	σ_{tot} = 35 mb [d]	0–0.18	good 8/8		1.29
De Pangher (44)	300 (284)	none	10 atmos. H_2 gas	Cloud chamber (10° bin size)			1	σ_{tot} = 35 mb	0–0.20	fair 16/7		1.23
Ashmore (45)	350 (344)	Downstream CH_2 target + range telescope	LH_2 (0.175)	Range in Cu + scintillator (1°) and (2°)			2 detectors	Refs. 44, 46, and 50 at 160° 40′	0–0.10	poor 160/15	fair 32/13	1.28
Dzhelepov [e] (50)	380 (378)	Proportional counter Bi fission	CH_2-C (?)	Proportional telescope (?)	?	?	?	σ_{tot} = 33 mb	0–0.15	fair		~1.3
Hartzler (46)	400 (414)	CH_2 target + range telescope	CH_2-C (2.15) CH_2-C (1.16) CH_2-C (0.58)	Range in Cu + scintillator (2°) (1°) (0.8°)	CH_2-C (?) LH_2 (?)	Converter + range in Cu + scintillator (2.2°)	5 targets 4 detectors	σ_{tot} = 33 mb	0–0.6	poor 93/16	poor	1.25
Kazarinov (47)	580 (541)	upstream unspecified	CH_2-C (5.0) CH_2-C (3.0) CH_2-C (0.5)	Range in Cu + scintillator (2°) [f]			3 targets 3 detectors	σ_{tot} = 26 mb [g]	0–0.9	poor 63/13	good 11/7 [h]	1.06
Amaglobeli (48)	630 (649)	upstream unspecified	CH_2-C (2.7) CH_2-C (0.9)	Range in W or Cu + scintillator (2°) (1°) [i]	LH_2 (?)	Converter + range + scintillator	3 targets 3 detectors	σ_{tot} = 25.8 mb	0–1.0	hopeless		
Larsen (49)	710 (649)	Proton flux on production target (Secondary emission)	LH_2 (?)	Scintillator + Čerenkov (?)			1	Absolute beam flux	0–0.5	fair 26/9		0.90

[a] In parentheses is the energy in our experiment at which comparisons were made.
[b] Thickness of range material is varied with angle.
[c] The authors suggest a 10% upward revision in the forward proton cross section because of resolution effects. That has been done for our calculation.
[d] A symmetric angular distribution was assumed.
[e] We have not found this work in translation.
[f] Additional measurements of pion and muon contamination with H_2O ($\theta_{lab} < 30°$) and Plexiglas ($30° < \theta_{lab} < 60°$) Čerenkov counters and by range ($\theta_{lab} > 60°$).
[g] $d\sigma/d\Omega$ was assumed constant from $\theta_{c.m.} = 0°$ to 35°.
[h] We have deleted the point for $\theta_{proton} = 0°$ and all points in the range covered by the Plexiglas Čerenkov counter.
[i] Pion and muon corrections were made on the basis of range ($\theta_{lab} > 60°$); or Čerenkov-counter data ($30° < \theta_{lab} < 60°$).

in these studies (Refs. 9, 12, 13, and 41–51). In Fig. 14(a) we plot the dimensionless quantity

$$(\hbar c)^{-2}(-t+m_\pi{}^2)(-u+m_\pi{}^2)\frac{d\sigma}{du} \text{ vs } (s-4M^2). \tag{4.1}$$

This is approximately proportional to the quantity plotted in Ref. 7 and displays the features observed there.

The function plotted is roughly independent of t and u in both shape and magnitude. Thus the features revealed in our earlier paper persist in the data up to $-u = 0.44$ and perhaps higher. This suggests that the source of the energy-dependent effect is not the one-pion-exchange contribution which is most important only in the region where $-u < 0.02$.

D. Comparison with total cross-section data

It is useful to consider the energy dependence of the difference between the proton-proton and neutron-proton total cross sections in connection with charge exchange scattering. Let us consider the optical theorem as it is usually applied to nucleon-nucleon scattering. We use a shorthand notation, f_j^I, to represent the forward scattering amplitude in a particular spin state j for isotopic spin I. The c.m. momentum is k. Then unitarity yields the following relationship between the total cross section and the spin-averaged forward scattering amplitude $\bar{f}^I$:

$$\sigma_{pp} = \frac{\pi}{k}\sum_{\text{nonflip}} \mathrm{Im}(f_j^1) \equiv \frac{4\pi}{k}\mathrm{Im}(\bar{f}^1). \tag{4.2}$$

The forward differential cross section is given by

$$\left.\frac{d\sigma_{pp}}{dt}\right|_{t=0} = \left.\frac{\pi}{k^2}\frac{d\sigma_{pp}}{d\Omega}\right|_{\theta=0} = \frac{\pi}{k^2}\sum_j |f_j^1|^2. \tag{4.3}$$

Similarly, for neutron-proton scattering

$$\sigma_{np} = \frac{4\pi}{k}\mathrm{Im}\tfrac{1}{2}(\bar{f}^1+\bar{f}^0), \tag{4.4}$$

$$\left.\frac{d\sigma_{np}}{dt}\right|_{t=0} = \frac{\pi}{k^2}\sum_j |\tfrac{1}{2}(f_j^1+f_j^0)|^2. \tag{4.5}$$

It is a simple matter to combine Eqs. (4.2) and (4.4) to yield

$$\sigma_{pp}-\sigma_{np} = \frac{4\pi}{k}\mathrm{Im}\tfrac{1}{2}(\bar{f}^1-\bar{f}^0). \tag{4.6}$$

In each state of well-defined total spin (singlet or triplet), the $I=0$ and $I=1$ amplitudes are *relatively* antisymmetric about $\theta = \frac{1}{2}\pi$. This allows us to write

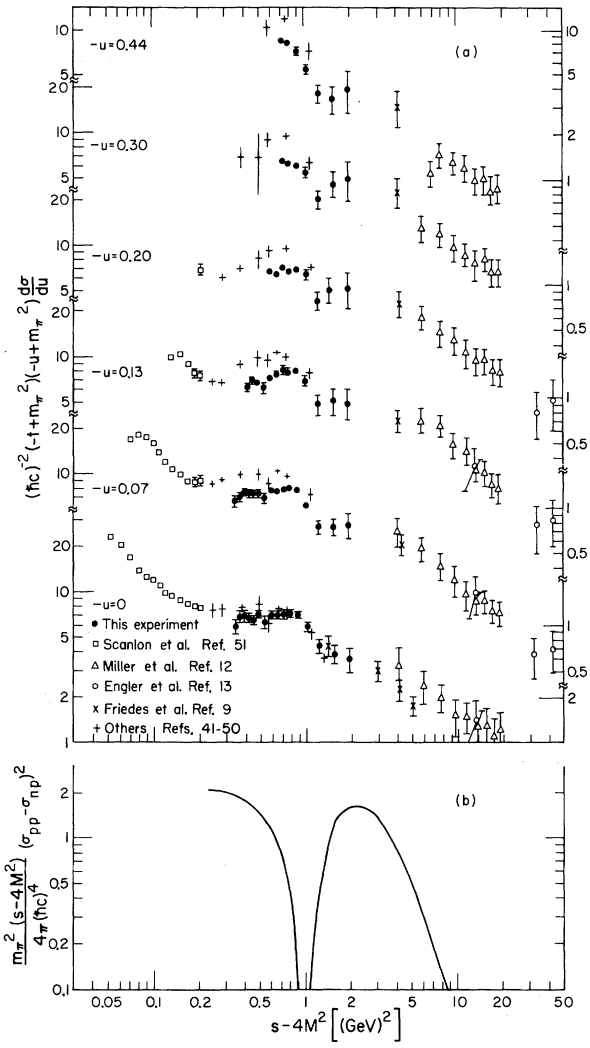

FIG. 14. (a) A graph of the dimensionless quantity $(\hbar c)^{-2}(-u+m_\pi{}^2)(-t+m_\pi{}^2)(d\sigma/du)$ vs $(s-4M^2)$ for various values of u. To an accuracy of order of the experimental errors, all the data are represented by a single function of s. (b) A graph of the square of the difference in total cross sections as a function of $(s-4M^2)$. (See text for discussion.)

$$\left.\frac{d\sigma_{np}}{du}\right|_{u=0} = \left.\frac{\pi}{k^2}\frac{d\sigma}{d\Omega}\right|_{\theta=\pi} = \frac{\pi}{k^2}\sum_j |\tfrac{1}{2}(f_j^1-f_j^0)|^2. \tag{4.7}$$

On a purely formal basis, the relationship between the total and differential cross sections expressed in Eqs. (4.6) and (4.7) is as valid as the more commonly applied versions of Eqs. (4.2)–(4.5). This gives us a "backward optical theorem." For practical purposes, it is less useful than the forward versions. There, the positive-definite imaginary parts of the amplitudes add to give the dominant

contribution to the differential cross sections. In the backward direction, they tend to cancel, yielding greater relative importance to those parts of the amplitudes not determined by the optical theorem. However, it still may be rewarding to look for correlations between dramatic energy dependent effects in these equantities.

In Fig. 14(b), we have plotted the dimensionless quantity

$$(4\pi)^{-1}(\hbar c)^{-4} m_\pi{}^2 (s - 4M^2)(\sigma_{pp} - \sigma_{np})^2 \quad \text{vs} \quad (s - 4M^2) \tag{4.8}$$

using data from Refs. 40 and 52. The coefficients were chosen to normalize this function in the same way as the $u = 0$ data of Fig. 14(a). The difference in the total cross sections shows a zero at the same energy as the deviation from smoothness in the charge-exchange cross section. No definite conclusion is forced on us, since it is possible for the average backward amplitude to be zero simply because of an accidental cancellation of the individual amplitudes. We merely suggest that there *may* be a connection. It is likely that a full phase-shift analysis is needed to confirm this.

ACKNOWLEDGMENTS

Thanks are due to Professor M. G. White, Professor A. Lemonick, and Professor W. D. Wales and the staff of the Princeton-Pennsylvania Accelerator for their hospitality and support during the execution and analysis of this experiment. We would like to thank Professor D. Miller, Dr. B. Ryan, and Dr. E. Cecil for their help during various stages of this work.

Mr. T. Droege and Mr. J. McFadden designed and built the spark-chamber readout system and computer interface. Mr. Ken Wright and his crew played a major role in the construction of the wire spark chambers. Mr. John Metzger and Mr. Victor Bearg wrote a number of the computer programs used in this work.

One of us (T.D.) is indebted to the National Science Foundation for support during the later stages of the analysis of the work.

During the analysis of the data, we made use of the facilities at the following computer centers: Princeton University, the Princeton-Pennsylvania Accelerator, CERN, Los Alamos Scientific Laboratory, the University of California at Los Angeles, and Rutgers University.

---

†Work supported in part by the U. S. Atomic Energy Commission under Contract No. AT(30-1)4159.

*Present address: Physics Department, University of Pittsburgh, Pittsburgh, Pennsylvania 15213.

‡Present address: Physics Department, Rutgers—The State University, New Brunswick, New Jersey 08903.

§Present address: MP Division, Los Alamos Scientific Laboratory, Los Alamos, New Mexico 87544.

‖Present address: Physics Department, University of Illinois, Chicago Circle, Chicago, Illinois 60680.

[1]M. H. MacGregor, R. A. Arndt, and R. M. Wright, Phys. Rev. 169, 1128 (1968).

[2]M. H. MacGregor, R. A. Arndt, and R. M. Wright, Phys. Rev. 169, 1149 (1968).

[3]M. H. MacGregor, R. A. Arndt, and R. M. Wright, Phys. Rev. 173, 1272 (1968).

[4]M. H. MacGregor, R. A. Arndt, and R. M. Wright, Phys. Rev. 182, 1714 (1969).

[5]R. E. Seamon, K. A. Friedman, G. Breit, R. D. Haracz, J. M. Holt, and A. Prakash, Phys. Rev. 165, 1579 (1968).

[6]G. Breit, Rev. Mod. Phys. 39, 560 (1967).

[7]R. E. Mischke, P. F. Shepard, and T. J. Devlin, Phys. Rev. Lett. 23, 542 (1969).

[8]P. F. Shepard, Ph.D. thesis, Princeton University, 1969 (unpublished); P. F. Shepard, T. J. Devlin, R. E. Mischke, and J. Solomon, Princeton-Pennsylvania Accelerator Report No. PPAR-10, 1969 (unpublished).

[9]J. L. Friedes, H. Palevsky, R. L. Stearns, and R. J. Sutter, Phys. Rev. Lett. 15, 38 (1965).

[10]G. Manning, A. G. Parham, J. D. Jafar, H. B. van der Raay, D. H. Reading, D. G. Ryan, B. D. Jones, J. Malos, and N. H. Lipman, Nuovo Cimento 41A, 167 (1966).

[11]R. Wilson, Ann. Phys. (N.Y.) 32, 193 (1965).

[12]E. L. Miller, M. Elfield, N. W. Reay, N. R. Stanton, M. A. Abolins, M. T. Lin, and K. W. Edwards, Phys. Rev. Lett. 26, 984 (1971).

[13]J. Engler, K. Horn, F. Mönnig, P. Schludecker, W. Schmidt-Parzefall, H. Schopper, P. Sievers, H. Ullrich, R. Hartung, K. Runge, and Yu. Galaktionov, Phys. Lett. 34B, 528 (1971).

[14]M. B. Davis, B. G. Gibbard, M. N. Kreisler, T. Dobrowolski, M. J. Longo, D. D. O'Brien, and T. Toohig, Phys. Rev. Lett. 29, 139 (1972).

[15]R. J. N. Phillips, Phys. Lett. 4, 19 (1963).

[16]M. M. Islam and T. W. Priest, Phys. Rev. Lett. 11, 444 (1963).

[17]G. A. Ringland and R. J. N. Phillips, Phys. Lett. 12, 62 (1964).

[18]E. M. Henley and I. J. Muzinich, Phys. Rev. 136B, 1783 (1964).

[19]J. S. Ball, A. Scotti, and D. Y. Wong, Phys. Rev. 142, 1000 (1966).

[20]E. Lomon and H. Feshbach, Rev. Mod. Phys. 39, 611 (1967).

[21]N. Byers, Phys. Rev. 156, 1703 (1967).

[22]F. Henyey, G. L. Kane, J. Pumplin, and M. H. Ross, Phys. Rev. 182, 1579 (1969).

[23]J. T. Londergan and R. M. Thaler, Phys. Rev. Lett. 25, 1065 (1970).

[24]R. A. Arndt and L. D. Roper, Phys. Rev. Lett. 26, 1260 (1971).

[25]T. Kitagaki, Princeton-Pennsylvania Accelerator

Technical Note No. A-215, 1965 (unpublished).
[26]M. W. Strovink, Princeton-Pennsylvania Accelerator Technical Note No. A-243, 1966 (unpublished).
[27]D. F. Bartlett, D. C. Cheng, C. E. Friedberg, K. Goulianos, I. Hammerman, and D. P. Hutchinson, Phys. Rev. D 1, 3087 (1970).
[28]During the first half of the running this polyethylene converter was not in the telescope.
[29]G. A. Sayer, E. F. Beall, T. J. Devlin, P. Shepard, and J. Solomon, Phys. Rev. 169, 1045 (1968).
[30]V. Perez-Mendez, T. J. Devlin, J. Solomon, and T. F. Droege, Nucl. Instrum. Meth. 46, 197 (1967).
[31]V. Perez-Mendez and J. M. Pfab, Nucl. Instrum. Meth. 33, 141 (1965).
[32]Thomas F. Droege, Princeton-Pennsylvania Accelerator Document No. PPAD 605-E, 1966 (unpublished).
[33]A detailed discussion of the on-line analysis is contained in the paper by R. E. Mischke, J. Metzger, P. F. Shepard, and T. J. Devlin [Princeton-Pennsylvania Accelerator Report No. PPAR-3, 1968 (unpublished)].
[34]We are indebted to J. Rosner and W. Y. Lau for calling our attention to this source of background.
[35]Paul E. Boynton, Princeton-Pennsylvania Accelerator Document No. PPAD-663F, 1967 (unpublished); P. E. Boynton, T. J. Devlin, J. Solomon, and V. Perez-Mendez, Phys. Rev. 174, 1083 (1968).
[36]T. J. Devlin, Univ. of California Lawrence Radiation Laboratory Report No. UCRL-9727, 1961 (unpublished).
[37]Marvin Rich and Richard Madey, Univ. of California Lawrence Radiation Laboratory Report No. UCRL-2301, 1964 (unpublished).
[38]The data are averaged over $800 \leq p \leq 1200$ MeV/c. Some error might be expected from this procedure. However, the decreasing efficiency with increasing bending angle is largely compensated for by vertical focusing effects. Therefore, the geometrical efficiency as a function of incident momentum at fixed scattering angle remains constant to $\sim 2\%$.
[39]B. A. Ryan, A. Kanofsky, T. J. Devlin, R. E. Mischke, and P. F. Shepard, Phys. Rev. D 3, 1 (1971).
[40]O. Benary, L. R. Price, and G. Alexander, Univ. of California Lawrence Radiation Laboratory Report No. UCRL-20000NN, 1970 (unpublished).
[41]D. F. Measday, Phys. Rev. 142, 584 (1966).
[42]Yu. M. Kazarinov and Yu. N. Simonov, Zh. Eksp. Teor. Fiz. 43, 35 (1962) [Sov. Phys.—JETP 16, 24 (1963)].
[43]E. Kelly, C. Leith, E. Segrè, and C. Wiegand, Phys. Rev. 79, 96 (1950).
[44]John De Pangher, Phys. Rev. 99, 1447 (1955).
[45]A. Ashmore, W. H. Range, R. T. Taylor, B. M. Townes, L. Castillejo, and R. F. Peierls, Nucl. Phys. 36, 258 (1962).
[46]A. J. Hartzler and R. T. Siegel, Phys. Rev. 95, 185 (1954); A. J. Hartzler, R. T. Siegel, and W. Opitz, *ibid.* 95, 591 (1954).
[47]Yu. M. Kazarinov and Yu. N. Simonov, Zh. Eksp. Teor. Fiz. 31, 169 (1956) [Sov. Phys.—JETP 4, 161 (1957)].
[48]N. S. Amaglobeli and Yu. M. Kazarinov, Zh. Eksp. Teor. Fiz. 37, 1587 (1959) [Sov. Phys.—JETP 10, 1125 (1960)].
[49]R. Larsen, Nuovo Cimento 18, 1039 (1960).
[50]Data quoted by W. N. Hess, Rev. Mod. Phys. 30, 368 (1958); V. P. Dzhelepov and Yu. M. Kazarinov, Dokl. Akad. Nauk. SSSR 99, 939 (1954); V. P. Dzhelepov, Yu. M. Kazarinov, B. M. Golovin, V. B. Flyagin, and V. I. Satarov, Izv. Akad. Nauk. SSSR 19, 573 (1955); and M. G. Meshcheryakov (private communication).
[51]J. P. Scanlon, G. H. Stafford, J. J. Thresher, P. H. Bowen, and A. Langsford, Nucl. Phys. 41, 401 (1963).
[52]T. J. Devlin, W. Johnson, J. Norem, K. Vosburgh, R. E. Mischke, and W. Schimmerling, Phys. Rev. D 8, 136 (1973).